https://doi.org/10.1130/G50315.1

Manuscript received 1 March 2022 Revised manuscript received 17 June 2022 Manuscript accepted 9 July 2022

Published online 5 September 2022

© 2022 Geological Society of America. For permission to copy, contact editing@geosociety.org

Cryogenian glacial erosion of the central Canadian Shield: The "late" Great Unconformity on thin ice

Kalin T. McDannell and C. Brenhin Keller

Department of Earth Sciences, Dartmouth College, Hanover, New Hampshire 03755, USA

ABSTRACT

The Great Unconformity has been recognized for more than a century, but only recently have its origins become a subject of debate. Hypotheses suggest global Snowball Earth glaciations and tectonic processes associated with the supercontinent Rodinia as drivers of widespread kilometer-scale erosion in the late Neoproterozoic. We present new integrated zircon and apatite (U-Th)/He and fission-track thermochronology from Precambrian basement samples of the central Canadian Shield in northern Manitoba to test these ideas. Bayesian inverse modeling indicates that 150–200 °C of cooling (>3 km of exhumation) occurred simultaneously with Cryogenian glaciations at ca. 690–650 Ma within interior North America. This estimate for the timing of unroofing is more precise than previous appraisals and does not align with any known tectonic or magmatic events (i.e., large igneous province eruptions) potentially associated with the supercontinent cycle that occurred during the late Proterozoic along the Laurentian margins. Based on these results and interpretations, the timing and magnitude of exhumation is best explained by glacial erosion, and further establishes the importance of multiple thermochronometers for resolving detailed deeptime thermal histories.

INTRODUCTION

Although unconformities are common in the geologic record, the profusion of unconformities shortly before the start of the Phanerozoic has long attracted attention (e.g., Walcott, 1914). This phenomenon, termed by some the "Great Unconformity", is represented physically as a series of temporally correlated, locally composite, but often profound unconformities, which, in the most typical case, superpose Precambrian crystalline basement with relatively undeformed Phanerozoic sedimentary rocks (Peters and Gaines, 2012; McDannell et al., 2022). Quantitatively, the Great Unconformity represents a fivefold step change in the global abundance of preserved sedimentary rock (Ronov et al., 1980). Despite its significance as arguably the most striking lacuna in the geologic record, the origin of the Great Unconformity remains debated (Keller et al., 2019; Flowers et al., 2020; Sturrock et al., 2021; McDannell et al., 2022). Recently, Keller et al. (2019) revived the glacial hypothesis of White (1973) and proposed that glacial erosion

during the Sturtian (717-659 Ma) and Marinoan (>641-635 Ma) Snowball Earth episodes (Hoffman et al., 2017) was responsible for the anomalous concentration of unconformities toward the end of the Precambrian. An alternate hypothesis argued for diachronous worldwide development of many "great unconformities" due to tectonic activity in the Neoproterozoic (Flowers et al., 2020). While thermochronology provides a valuable potential test for these hypotheses, the temporal and spatial patterns of Neoproterozoic exhumation must be constrained accurately, focusing on regions that were not experiencing tectonism if we are to judge the timing and extent of glacial versus tectonic contributions to the Great Unconformity (McDannell et al., 2022).

Neoproterozoic exhumation and "late" (post-650 Ma) unconformity formation in the central Canadian Shield were attributed by Sturrock et al. (2021) to either Marinoan glaciation or various tectonic drivers, including their preferred interpretation of uplift and erosion from mantle plume dynamics and Laurentian margin

rifting. One possible source of ambiguity for the timing and cause of rock cooling is that Sturrock et al. applied only the apatite (U-Th)/He (AHe) thermochronometer. The AHe system is sensitive to low temperatures (\sim 80–50 °C), and dates are often partially overprinted by Phanerozoic burial heating in cratonic settings (for review, see Kohn and Gleadow [2019]). As a result, AHe data in isolation can be problematic for resolving the timing of initial cooling from elevated temperatures (see Figs. S1-S3 in the Supplemental Material¹). Individual chronometers account for only a partial record of the time-temperature (t-T) history, and different biases and uncertainties affect model thermal history recovery, including inherent temperature sensitivity, diffusion/annealing model calibrations, elemental heterogeneity, and random sampling (i.e., grain selection). Studies involving data from one thermochronometer can be instructive, but the use of multiple chronometers provides a means of exploring a broader t-T history and yields betterconstrained model outputs, particularly when analyzing samples within a deep-time context (McDannell et al., 2019; McDannell and Flowers, 2020).

We investigated these emergent North American denudation patterns by integrating and modeling new thermochronologic data from the central Canadian Shield, and assess the claim of a "late" unconformity for the stable interior. We applied multi-system thermochronology using newly reported data from two basement samples (Fig. 1) from the western margin of Hudson Bay in northern Manitoba, Canada (samples 97-10-481 [58.69435473°N, 95.11097964°W] and 97-10-499 [58.73422417°N, 94.97797088°W], hereafter referred to as S481 and S499; see the Supplemental Material). The timing of Neoproterozoic exhumation within the continental

CITATION: McDannell, K.T., and Keller, C.B., 2022, Cryogenian glacial erosion of the central Canadian Shield: The "late" Great Unconformity on thin ice: Geology, v. XX, p. , https://doi.org/10.1130/G50315.1

¹Supplemental Material. Supporting text, figures, and analytical data. Please visit https://doi.org/10.1130/GEOL.S.20503476 to access the supplemental material, and contact editing@geosociety.org with any questions.

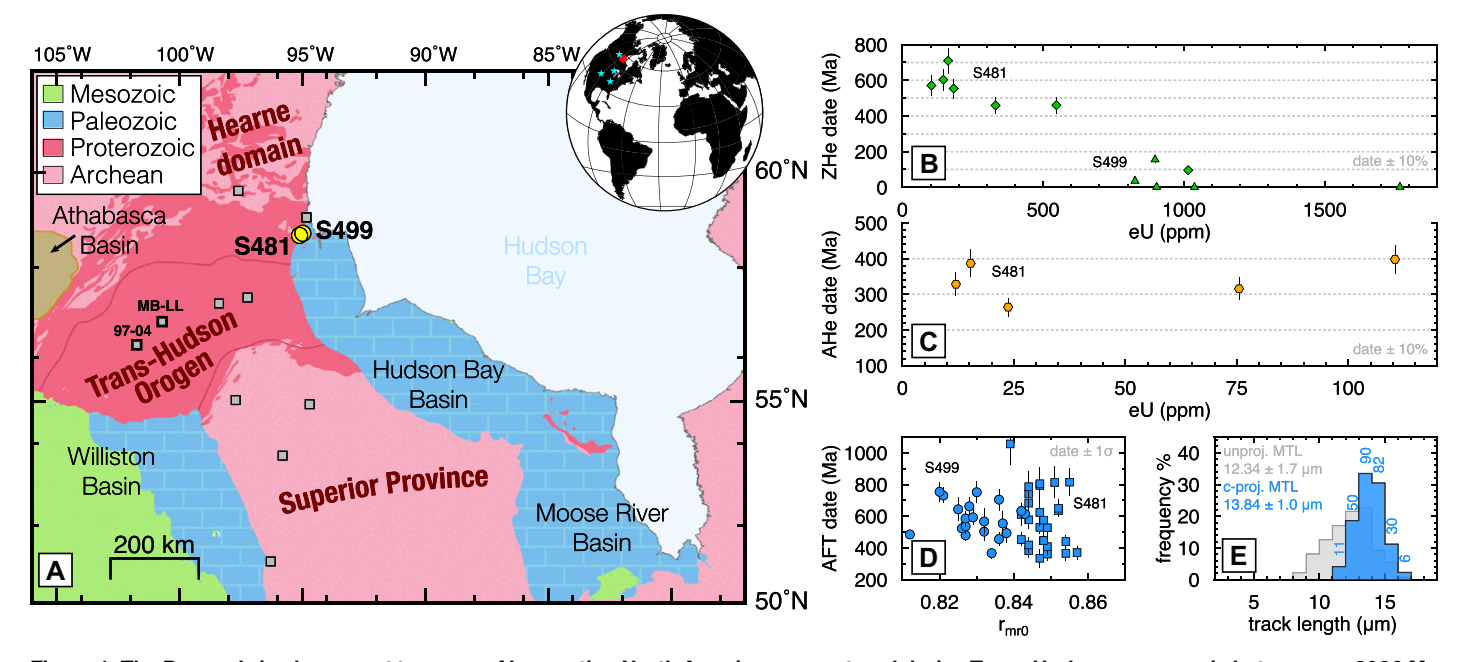


Figure 1. The Precambrian basement terranes of Laurentian North America were sutured during Trans-Hudson orogenesis between ca. 2000 Ma and 1800 Ma (Hoffman, 1988). The oldest Phanerozoic strata overlying Precambrian basement represent the end of the Great Unconformity. Thus, the surface evolution of the central shield is poorly known in detail between ca. 1800 Ma and 500 Ma. Remnant intracratonic basins demonstrate that the region was intermittently buried by sedimentary rocks during the Proterozoic (e.g., Athabasca Basin at 1.7 Ga), early Paleozoic, and late Mesozoic. This general pattern is corroborated by existing thermochronology (for review, see Kohn and Gleadow [2019]). (A) Simplified geology of the central Canadian Shield, showing basement sample locations (Wheeler et al., 1996). New samples presented in this paper and those from Sturrock et al. (2021) are shown by circles and squares, respectively. Sturrock et al. (2021) samples MB-LL and 97–04 are discussed in the Supplemental Material (see footnote 1). Inset map shows samples (stars) from McDannell et al. (2022). (B,C) New, corrected zircon (U–Th)/He (ZHe) and apatite (U–Th)/He (AHe) data displayed on date-eU (effective uranium) plots. (D) Apatite fission-track (AFT) single-grain dates plotted with respect to the r_{mro} kinetic parameter (fluorapatite r_{mro} ~0.83–0.84). (E) Measured AFT length distribution for samples S481 and S499 (combined).

interior is better constrained by zircon (U-Th)/ He (ZHe), apatite fission-track (AFT), and AHe thermochronology with combined sensitivities of \sim 220–30 °C. An inverse t-T simulation reveals >3 km of interpreted cratonic unroofing that is synchronous with the Sturtian and Marinoan glaciations.

INTEGRATED THERMOCHRONOLOGY AND INVERSE THERMAL HISTORY MODELING

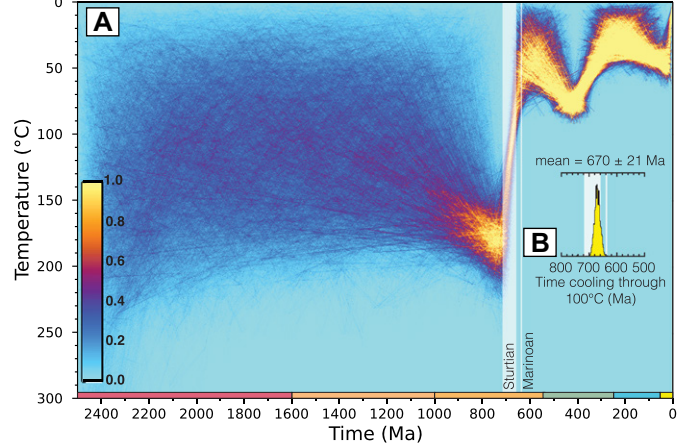
Samples S481 (hornblende granite) and S499 (foliated granodiorite) were collected from Neoarchean basement in the Seal River region of northern Manitoba (Anderson et al., 2010; Fig. 1A). The samples are \sim 9 km from one another and \sim 1–6 km from the basement contact with overlying Late Ordovician carbonates. This datum provides an important geologic constraint because most of the central Canadian Shield is devoid of Phanerozoic cover (Fig. 1). (U-Th)/He data were analyzed at the University of Calgary (Canada; ZHe) and the University of Colorado Boulder (USA; AHe). The ZHe and AHe data were acquired using the analytical methods of McKay et al. (2021) and Sturrock et al. (2021), respectively. Analyst P. O'Sullivan (GeoSep Services, Idaho, USA) collected the AFT data, following the methods of McDannell et al. (2019). Together, the S481 and S499 zircons display a negative date-effective uranium trend (eU = U + 0.238 × Th), and alpha ejection-corrected dates span ca. 710 Ma to <1 Ma (n=12) over $\sim 100-1765$ ppm eU (Fig. 1B; Table S1). Corrected AHe dates for S481 range from ca. 250 to 400 Ma (n=5) over $\sim 15-110$ ppm eU (Fig. 1C; Table S2). The AFT data from both samples (Tables S3–S5) were merged due to statistically indistinguishable apparent ages and track length distributions and similar annealing kinetics, yielding 47 single-grain ages with a central age of 563 ± 42 Ma (2σ) and a c axis-projected mean track length (MTL) of $13.84 \pm 1.06 \,\mu m$ (n=269) (Figs. 1D and 1E).

We used the QTQt software (v. 5.8.0; http:// iearth.edu.au/codes/QTQt/; Gallagher, 2012) for inverse modeling of the integrated data via the methods discussed by McDannell et al. (2022). Contrary to many published studies, our inversion does not impose a priori an interpretive geologic model (i.e., independent t-T "constraint boxes" were not applied). The thermal history model was instead validated by the geology (Fig. 2A). The Ordovician nonconformity is the only robust physical geologic constraint for these samples. Age uncertainty quantification was also investigated, because (U-Th)/He analytical uncertainties often greatly underestimate the true external uncertainty due to currently unexplained sources of dispersion.

The total uncertainty was conservatively set to 10% for both the ZHe dates and the AHe dates, while the ZHe uncertainties were resampled (1–100 × input error) using Hierarchical Bayes methods in OTOt (McDannell et al., 2022). The ZHe and AHe kinetic models of Guenthner et al. (2013) and Flowers et al. (2009) were utilized, while the elemental chemistry for the AFT data was used to infer implicit kinetic variability in the AHe data (McDannell and Issler, 2021). The r_{mol} kinetic parameter is used to quantify damage annealing in apatite (i.e., 4He retentivity; Flowers et al., 2009) and was resampled for each individually modeled S481 apatite (r_{mr0} represents a measure of the relative resistance to track annealing compared to the most retentive apatite in published annealing experiments).

Model Results and Interpretations

Our *t-T* model exhibits a poorly resolved Proterozoic history except for the requirement of reheating to \sim 150–200 °C by 1000–700 Ma. Maximum heating is followed by relatively rapid \sim 2 °C/m.y. cooling through \sim 100 °C at ca. 670 \pm 21 Ma (2 σ) during the Sturtian cryochron (Figs. 2A and 2B; Fig. S4) and is coincident with the timing of Laurentian deglaciation at 662 \pm 4 Ma (Rooney et al., 2014). This result also agrees with the published thermal history of the nearby Athabasca



ice and glacial fluctuations (e.g., Condon et al., 2002; Eyles et al., 2007; Fleming et al., 2016). Critically, basal sliding and ice streams would have denuded sedimentary rocks and caused appreciable basement erosion throughout the glaciated continental interior, whereas tectonic uplift and unroofing would be restricted mainly to orogenic belts and rift flanks. While Rodinian tectonics and associated magmatism may have initiated the Sturtian glaciation (Goddéris et al., 2003), our modeling suggests that significant Neoproterozoic erosion specifically coincided with Cryogenian glaciation rather than being distributed throughout the much more protracted intervals of Rodinian assembly or breakup in North America. We therefore favor the interpretation that kilometers of rock exhumation during the Cryogenian are most parsimoniously explained by glacial erosion, consistent with existing geochemical (Keller et al., 2019) and thermochronological (McDannell et al., 2022) evidence.

CONCLUSIONS

Our inverse thermal history model integrates multiple thermochronometers (ZHe, AFT, and AHe data) and indicates that the central Canadian Shield experienced a pronounced cooling event that we interpret as >3 km of exhumation in the Neoproterozoic. Exhumation occurred at ca. 670 ± 21 Ma, coincident with Cryogenian glaciation. Considering the diachroneity with known magmatic events and the absence of evidence for tectonic deformation in the shield interior thousands of kilometers from the thenactive margins, we regard basal sliding of a continental ice sheet, which is expected across the low-latitude continental interiors in the Cryogenian (Donnadieu et al., 2003), to represent the most plausible known erosive mechanism at this locality.

ACKNOWLEDGMENTS

This work was partially supported by U.S. National Science Foundation EAR-SGP award 2044800. The Government of Canada GEM-2 Program funded K. McDannell and contracted analyses (2017–2020). N. Pinet, C. Böhm, and the Manitoba Geological Survey are thanked for providing samples and context. We thank reviewers C. Willett, J. Powell, and D. Foster for comments that improved the manuscript.

REFERENCES CITED

- Anderson, S., Böhm, C., and Syme, E., 2010, Far North Geomapping Initiative: Bedrock geological investigations in the Seal River region, northeastern Manitoba (parts of NTS 54L, M, 64I, P), *in* Report of Activities 2010: Manitoba Innovation, Energy and Mines, Manitoba, Canada, Manitoba Geological Survey, p. 6–22, https://www.manitoba.ca/iem/geo/field/roa10pdfs/GS-1.pdf.
- Braun, J., Robert, X., and Simon-Labric, T., 2013, Eroding dynamic topography: Geophysical Research Letters, v. 40, p. 1494–1499, https://doi .org/10.1002/grl.50310.
- Burgess, P.M., 2019, Phanerozoic evolution of the sedimentary cover of the North American Cra-

- ton, *in* Miall, A.D., ed., The Sedimentary Basins of the United States and Canada (2nd edition): Amsterdam, Elsevier, p. 39–75, https://doi.org/10.1016/B978-0-444-63895-3.00002-4.
- Cawood, P.A., McCausland, P.J., and Dunning, G.R., 2001, Opening Iapetus: Constraints from the Laurentian margin in Newfoundland: Geological Society of America Bulletin, v. 113, p. 443–453, https://doi.org/10.1130/0016-7606(2001)113<0443:OIC FTL>2.0.CO;2.
- Condon, D.J., Prave, A.R., and Benn, D.I., 2002, Neoproterozoic glacial-rainout intervals: Observations and implications: Geology, v. 30, p. 35–38, https://doi.org/10.1130/0091-7613(2002)030<0035:NG RIOA>2.0.CO;2.
- Cowton, T., Nienow, P., Bartholomew, I., Sole, A., and Mair, D., 2012, Rapid erosion beneath the Greenland ice sheet: Geology, v. 40, p. 343–346, https://doi.org/10.1130/G32687.1.
- Donnadieu, Y., Fluteau, F., Ramstein, G., Ritz, C., and Besse, J., 2003, Is there a conflict between the Neoproterozoic glacial deposits and the snowball Earth interpretation: An improved understanding with numerical modeling: Earth and Planetary Science Letters, v. 208, p. 101–112, https://doi.org/10.1016/S0012-821X(02)01152-4.
- Ernst, R.E., Bond, D.P.G., Zhang, S., Buchan, K.L., Grasby, S.E., Youbi, N., El Bilali, H., Bekker, A., and Doucet, L.S., 2021, Large igneous province record through time and implications for secular environmental changes and geological time-scale boundaries, *in* Ernst, R.E., et al., eds., Large Igneous Provinces: A Driver of Global Environmental and Biotic Changes: American Geophysical Union Geophysical Monograph 255, p. 1–26, https://doi.org/10.1002/9781119507444.ch1.
- Eyles, C.H., Eyles, N., and Grey, K., 2007, Palaeoclimate implications from deep drilling of Neoproterozoic strata in the Officer Basin and Adelaide Rift Complex of Australia; A marine record of wet-based glaciers: Palaeogeography, Palaeoclimatology, Palaeoecology, v. 248, p. 291–312, https://doi.org/10.1016/j.palaeo.2006.12.008.
- Feinstein, S., Kohn, B., Osadetz, K., Everitt, R., and O'Sullivan, P., 2009, Variable Phanerozoic thermal history in the Southern Canadian Shield: Evidence from an apatite fission track profile at the Underground Research Laboratory (URL), Manitoba: Tectonophysics, v. 475, p. 190–199, https://doi.org/10.1016/j.tecto.2009.01.016.
- Fleming, E.J., Benn, D.I., Stevenson, C.T., Petronis, M.S., Hambrey, M.J., and Fairchild, I.J., 2016, Glacitectonism, subglacial and glacilacustrine processes during a Neoproterozoic panglaciation, north-east Svalbard: Sedimentology, v. 63, p. 411–442, https://doi.org/10.1111/sed.12251.
- Flowers, R.M., Ketcham, R.A., Shuster, D.L., and Farley, K.A., 2009, Apatite (U–Th)/He thermochronometry using a radiation damage accumulation and annealing model: Geochimica et Cosmochimica Acta, v. 73, p. 2347–2365, https://doi.org/10.1016/j.gca.2009.01.015.
- Flowers, R.M., MacDonald, F.A., Siddoway, C.S., and Havranek, R., 2020, Diachronous development of Great Unconformities before Neoproterozoic Snowball Earth: Proceedings of the National Academy of Sciences of the United States of America, v. 117, p. 10,172–10,180, https://doi.org/10.1073/pnas.1913131117.
- Gallagher, K., 2012, Transdimensional inverse thermal history modeling for quantitative thermochronology: Journal of Geophysical Research: Solid Earth, v. 117, B02408, https://doi.org/10.1029/2011JB008825.
- Goddéris, Y., Donnadieu, Y., Nédélec, A., Dupré, B., Dessert, C., Grard, A., Ramstein, G., and François, L.M., 2003, The Sturtian 'snowball' glacia-

- tion: Fire and ice: Earth and Planetary Science Letters, v. 211, p. 1–12, https://doi.org/10.1016/S0012-821X(03)00197-3.
- Guenthner, W.R., Reiners, P.W., Ketcham, R.A., Nasdala, L., and Giester, G., 2013, Helium diffusion in natural zircon: Radiation damage, anisotropy, and the interpretation of zircon (U-Th)/He thermochronology: American Journal of Science, v. 313, p. 145–198, https://doi.org/10.2475/03.2013.01.
- Hallet, B., Hunter, L., and Bogen, J., 1996, Rates of erosion and sediment evacuation by glaciers: A review of field data and their implications: Global and Planetary Change, v. 12, p. 213–235, https://doi.org/10.1016/0921-8181(95)00021-6.
- Herman, F., Seward, D., Valla, P.G., Carter, A., Kohn, B., Willett, S.D., and Ehlers, T.A., 2013, Worldwide acceleration of mountain erosion under a cooling climate: Nature, v. 504, p. 423–426, https://doi.org/10.1038/nature12877.
- Hoffman, P.F., 1988, United plates of America, the birth of a craton: Early Proterozoic assembly and growth of Laurentia: Annual Review of Earth and Planetary Sciences, v. 16, p. 543–603, https://doi.org/10.1146/annurev.ea.16.050188.002551.
- Hoffman, P.F., et al., 2017, Snowball Earth climate dynamics and Cryogenian geology-geobiology: Science Advances, v. 3, https://doi.org/10.1126/ sciadv.1600983.
- Keller, C.B., Husson, J.M., Mitchell, R.N., Bottke, W.F., Gernon, T.M., Boehnke, P., Bell, E.A., Swanson-Hysell, N.L., and Peters, S.E., 2019, Neoproterozoic glacial origin of the Great Unconformity: Proceedings of the National Academy of Sciences of the United States of America, v. 116, p. 1136–1145, https://doi.org/10.1073/ pnas.1804350116.
- Kohn, B., and Gleadow, A., 2019, Application of low-temperature thermochronology to craton evolution, in Malusá, M.G., and Fitzgerald, P.G., eds., Fission-Track Thermochronology and its Application to Geology: Cham, Switzerland, Springer, p. 373–393, https://doi.org/10.1007/978-3-319-89421-8_21.
- McClellan, E., and Gazel, E., 2014, The Cryogenian intra-continental rifting of Rodinia: Evidence from the Laurentian margin in eastern North America: Lithos, v. 206–207, p. 321–337, https://doi.org/10.1016/j.lithos.2014.08.006.
- McDannell, K.T., and Flowers, R.M., 2020, Vestiges of the ancient: Deep-time noble gas thermochronology: Elements, v. 16, p. 325–330, https://doi.org/10.2138/gselements.16.5.325.
- McDannell, K.T., and Issler, D.R., 2021, Simulating sedimentary burial cycles Part 1: Investigating the role of apatite fission track annealing kinetics using synthetic data: Geochronology, v. 3, p. 321–335, https://doi.org/10.5194/gchron-3-321-2021.
- McDannell, K.T., Schneider, D.A., Zeitler, P.K., O'Sullivan, P.B., and Issler, D.R., 2019, Reconstructing deep-time histories from integrated thermochronology: An example from southern Baffin Island, Canada: Terra Nova, v. 31, p. 189–204, https://doi.org/10.1111/ter.12386.
- McDannell, K.T., Keller, C.B., Guenthner, W.R., Zeitler, P.K., and Shuster, D.L., 2022, Thermochronologic constraints on the origin of the Great Unconformity: Proceedings of the National Academy of Sciences of the United States of America, v. 119, https://doi.org/10.1073/pnas.2118682119.
- McKay, R., Enkelmann, E., Hadlari, T., Matthews, W., and Mouthereau, F., 2021, Cenozoic exhumation history of the eastern margin of the Northern Canadian Cordillera: Tectonics, v. 40, https://doi.org/10.1029/2020TC006582.
- Peters, S.E., and Gaines, R.R., 2012, Formation of the 'Great Unconformity' as a trigger for the

- Cambrian explosion: Nature, v. 484, p. 363–366, https://doi.org/10.1038/nature10969.
- Ronov, A.B., Khain, V.E., Balukhovsky, A.N., and Seslavinsky, K.B., 1980, Quantitative analysis of Phanerozoic sedimentation: Sedimentary Geology, v. 25, p. 311–325, https://doi.org/10.1016/0037-0738(80)90067-6.
- Rooney, A.D., Macdonald, F.A., Strauss, J.V., Dudás, F.O., Hallmann, C., and Selby, D., 2014, Re-Os geochronology and coupled Os-Sr isotope constraints on the Sturtian snowball Earth: Proceedings of the National Academy
- of Sciences of the United States of America, v. 111, p. 51–56, https://doi.org/10.1073/pnas.1317266110.
- Sturrock, C.P., Flowers, R.M., and Macdonald, F.A., 2021, The late Great Unconformity of the Central Canadian Shield: Geochemistry Geophysics Geosystems, v. 22, https://doi.org/10.1029/2020GC009567.
- Walcott, C.D., 1914, Cambrian Geology and Paleontology: Smithsonian Miscellaneous Collections, Volume 57: Baltimore, Maryland, The Lord Baltimore Press, 412 p.
- Wheeler, J.O., Hoffman, P., Card, K., Davidson, A., Sanford, B.V., Okulitch, A., and Roest, W., compilers, 1996, Geological map of Canada / Carte géologique du Canada: Geological Survey of Canada, scale: 1:5,000,000, 1 sheet, https://doi .org/10.4095/208175.
- White, W.A., 1973, Deep erosion by Infracambrian ice sheets: Geological Society of America Bulletin, v. 84, p. 1841–1843, https://doi.org/10.1130/0016-7606(1973)84<1841:DEBIIS>2.0.CO;2.

Printed in USA

McDannell, K.T., and Keller, C.B., 2022, Cryogenian glacial erosion of the central Canadian Shield: The "late" Great Unconformity on thin ice: Geology, v. 50, https://doi.org/10.1130/G50315.1

Supplemental Material for

Cryogenian glacial erosion of the central Canadian Shield: The "late" Great Unconformity on thin ice

Kalin T. McDannell and C. Brenhin Keller

Correspondence may be addressed to: Kalin McDannell e-mail: kalin.t.mcdannell@dartmouth.edu

This PDF file includes:

Supplementary text Figs. S1 to S5 Tables S1 to S5 SI References

Supporting Information Text

This document contains the analytical data and supporting text/figures for the publication: Cryogenian glacial erosion of the central Canadian Shield: The "late" Great Unconformity on thin ice by K.T. McDannell and C.B. Keller. Figures S1, S2, and S3 elaborate on the Sturrock et al. (1) results and Figures S4 and S5 support the QTQt results in the main paper. Sample locations (decimal degrees). 97-10-481 » latitude: 58.69435473, longitude: -95.11097964 (hornblende granite, massive; near North Knife River). 97-10-499 » latitude: 58.73422417, longitude: -94.97797088 (granodiorite, foliated-gneissic; near Nowell Lake). Refer to Anderson et al. (2, 3) and Rayner (4) for details on the local geology.

Thermochronometer sensitivity: Comparing multi-system thermochronology and single low-temperature thermochronometer inversions. A critical outcome that is reinforced in this work is that multiple thermochronometers are required to constrain deep-time histories (5). The following insights are provided within the context of an inverse modeling approach driven fundamentally by the information contained in unified thermochronological systems. These points are specific to the aim of constraining cooling from high-temperatures in deep-time inversions assessing interpreted Neoproterozoic exhumation. Ideally, single-grain dates from the zircon (U-Th)/He (ZHe) and apatite (U-Th)/He (AHe) methods should span the entire range of eU (i.e., low-eU zircons and high-eU apatites are critical). Apatite fission-track (AFT) samples must be replete with > 100 track-length measurements and of sufficient retentivity to contain at least a partial record of initial cooling if later heating events occurred (i.e., not thermally reset). Exploiting inter-chronometer sensitivities and leveraging system trade-offs are ways to determine viable time-temperature (t-T) solutions common to all of the input data (5, 6).

The use of interpretative constraints (usually imposed as t-T "exploration boxes") also affect deep-time thermal history recovery, and in these situations, the influence of constraint boxes on the t-T model results must be assessed with respect to the resolving power of the data (e.g., 5, 7–10). The use of t-T boxes for modeling thermochronological data that lack sensitivity to specific portions of the thermal history can imply a history is well-constrained by the data (10, for discussion). This is relevant for cratonic scenarios where attempts are made to identify cooling events from elevated temperatures using only a single low-temperature thermochronometer that does not possess adequate t-T information to clearly resolve such events (e.g., 1). For example, high-eU (> 80–150 ppm) apatite grains are more resistant to thermal resetting and thus most sensitive to initial cooling from high temperatures (Fig. S1A–B). The AHe thermochronometer will have poor t-T resolution if the number of modeled single-grain dates is low and if analyses do not encompass the high-eU grains (Fig. S1C). Models will also be biased towards apparently "younger" or "late" cooling if the true temperature from which cooling begins is substantially greater (and/or earlier) than the effective AHe closure temperature, since only the later, low-temperature portion of the history will be retained (see Fig. S2 and Fig. S3 below). These subtle but significant effects are made worse for cases where individual AHe dates are binned by eU and averaged and the assigned uncertainties are large (e.g., ref. 1; Fig. S1D; 10, for discussion).

The Sturrock et al. (1) regional AHe data yield similar date-eU trends and random Monte Carlo models show a broadly consistent monotonic-cooling history during the Neoproterozoic. Their thermal history results (their Figs. 4 and 5) exhibit paths that connect a high-temperature box (based on regional thermochronologic information; 11) to a low-temperature box derived from the geologic requirement of Precambrian basement being at surface by the Ordovician. When viewed within the context of a statistically acceptable suite of t-T solutions, rather than focusing on a single path, a distinctive 650–450 Ma cooling trend is not apparent. The envelope of their "acceptable" 0.05 solutions generally show cooling to surface could have occurred at any time between 800 Ma and 440 Ma and the cooling trajectory is simply due to the high and low-temperature t-T boxes. This suggests that there is a lack of t-T resolution (and data) to provide robust support for either Great Unconformity formation hypothesis (i.e., glaciation or tectonics), which was indirectly echoed in their discussion and conclusions (1)—yet cursory preference was given to a tectonic cause for the unconformity.

An additional consideration is that the widely used a patite radiation damage kinetic model for He diffusion (12) is not well calibrated at high effective fission-track densities (i.e., old/high-U apatites). This implies He diffusivity may be poorly constrained for such grains and would be most problematic in ancient settings, especially when attempting to constrain cooling from high temperatures with fidelity. Some of the Sturrock et al. (1) AHe data exhibit a decrease in age at high eU (Fig. S1A), potentially signifying a transition to enhanced He diffusivity for grains that have interconnected radiation damage (13, 14). While rarely documented, this behavior may be more common for old apatites (15) and warrants further scrutiny since it is not well explained by current kinetic models. The cumulative effect of these factors calls into question the reliability of deep-time t-T interpretations based solely on AHe data.

To further demonstrate the limited sensitivity of AHe data modeled in isolation, we show a HeFTy (16) inversion similar in setup to the models presented in Sturrock et al. (1) (their Fig. 4). Given the poorly known total age uncertainties for cratonic AHe data and the unknown timing of basement exhumation prior to 480–440 Ma (regional Ordovician deposition), the observed single-grain AHe dates for combined samples MB-LL and 97-04 (10% applied uncertainties) can be explained equally well by either indistinct monotonic Neoproterozoic cooling followed by Paleozoic heating, or by only Paleozoic and/or Mesozoic heating event(s) (Fig. S2). An alternate model is shown here with an open t-T box configuration (Fig. S3) and demonstrates that from 1000–700 Ma there is very poor resolution. Paths oscillate between heating and cooling from ca. 700–600 Ma, but generally exhibit cooling that starts anywhere between \sim 200–60°C, implying that there is poor-to-moderate t-T resolution in this interval. The 600–480 Ma box is the only region of Precambrian t-T space that demonstrates a consistent cooling signal—this suggests that sensitivity is restricted to temperatures < 70–80°C and < 600 Ma (gray shading). Therefore, the observed "late" cooling is more due to the onset of AHe sensitivity and model assumptions (i.e., t-T boxes). Their AHe data lack adequate resolution to distinguish between the unconformity hypotheses (Fig. S3).

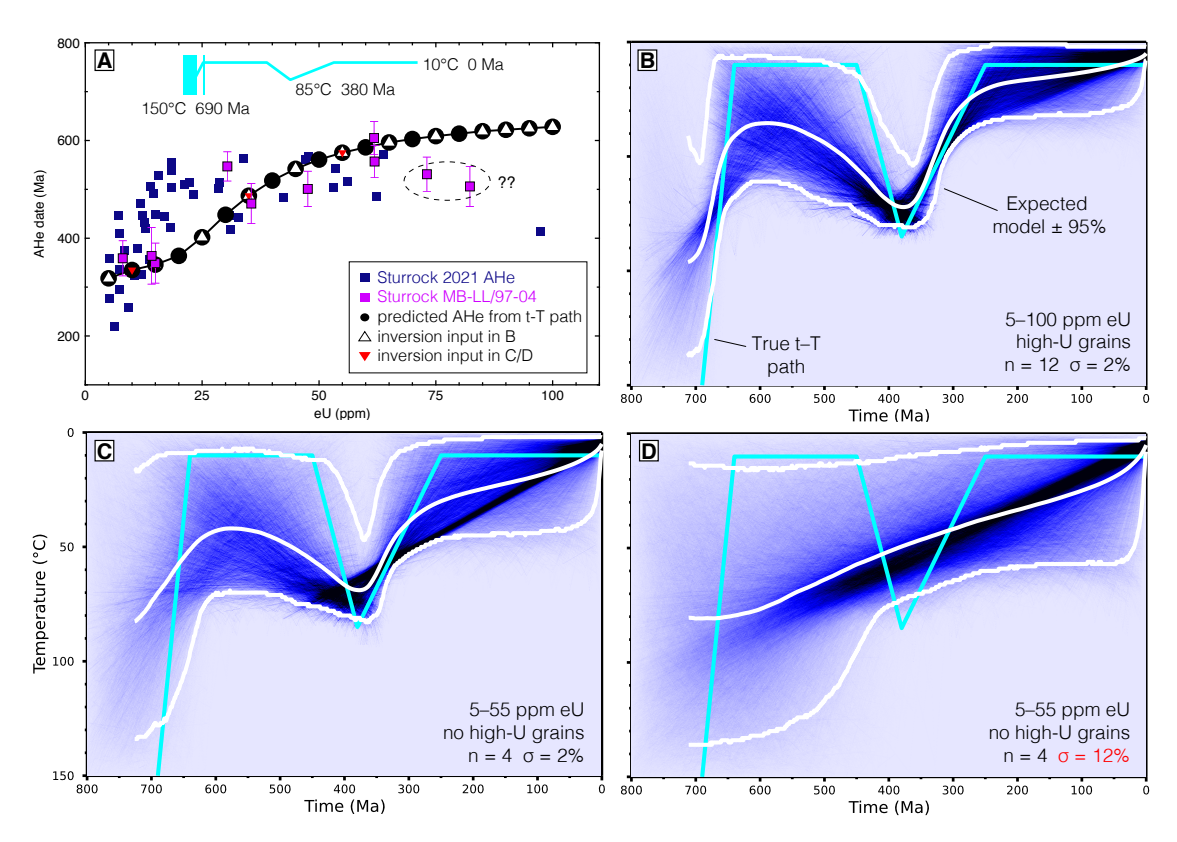


Fig. S1. Evaluation of central Canadian Shield apatite (U–Th)/He data trends. **(A)** Sturrock et al. (1) AHe dataset shown (light blue squares) with a focus on their samples MB-LL/97-04 within the Trans-Hudson Orogen (see Fig. 1 location map in main text). Simplified thermal history (cyan path) characterized by 690–640 Ma cooling from 150°C during Cryogenian glaciations and reheating during the Paleozoic. Black points are predicted AHe dates from that t–T path using the radiation damage model of Flowers et al. (12). Apatites were set to 50 μ m spherical radius and span 5–100 ppm eU. Note the close similarity between the predicted dates for the schematic Cryogenian cooling history and the observed MB-LL/97-04 AHe data (magenta squares). Panels (B–D) show inversions of those data in QTQt without constraint boxes to recover the main features of the t–T path in panel A (i.e., initial cooling and reheating event; AHe data are insensitive to low-temperature history segments). Plot shows a heat map of path density resolved to a pixel size of 1 Myr and 1°C. Relative probability is proportional to path density, where darker colors and/or higher saturation indicate more accepted thermal histories pass through that region of t–T space. The Expected model or posterior weighted average of accepted paths (\pm 95% credible interval) is shown to indicate overall resolution trends. (B) Inversion of AHe dates spanning entire eU range with a focus on oldest grains (white triangles in panel A). Sensitivity is limited to <75°C for initial cooling pulse. (C) Inversion with only 4 grains (5–55 ppm eU; red inverted triangles in panel A). Timing of cooling is poorly resolved. (D) Same inversion as in C but uncertainties were set to 12% of the observed age, as in Sturrock et al. (1). There is complete loss of resolution that would require many interpretive t–t boxes to find suitable paths that are geologically reasonable. Such an inversion would thus be entirely controlled by, and based on, the interpretive geologic

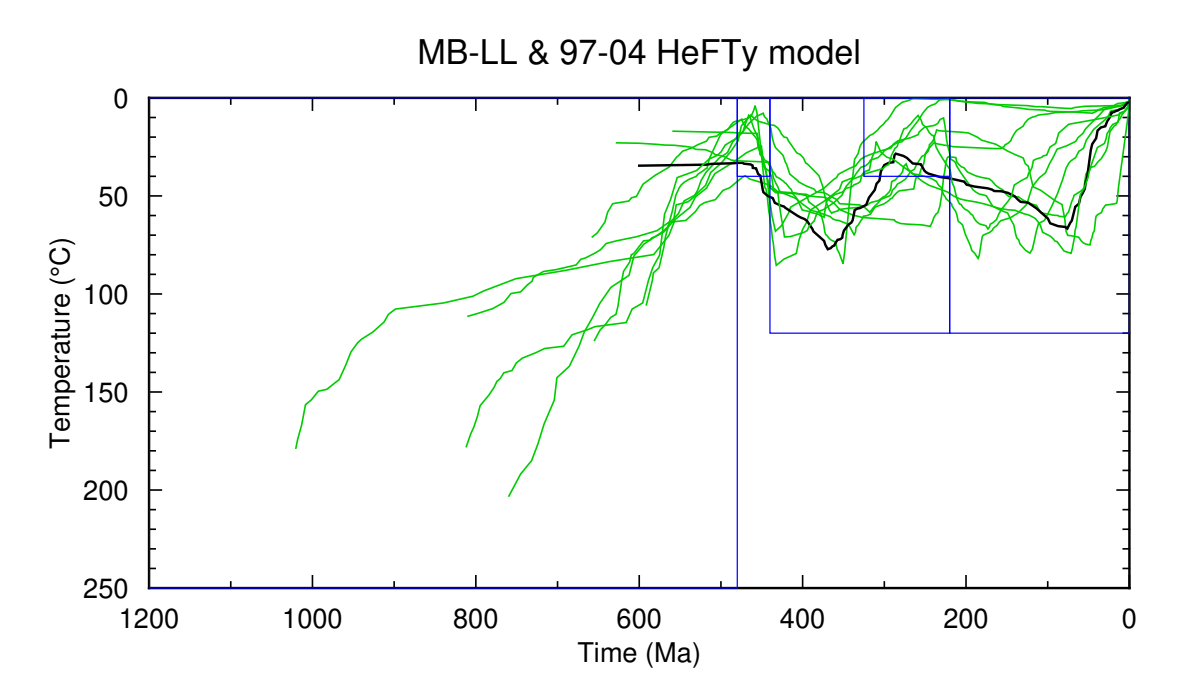


Fig. S2. Inversion of the Sturrock et al. (1) samples MB-LL and 97-04-7066 from the Trans-Hudson Orogen (their Fig. 4) using the HeFTy software v.1.9.3 (16). We modeled only 7 single-grain AHe dates from the samples (the maximum single-grain inputs allowed for HeFTy) and set the errors at 10% of the corrected age, including MB-LL grains a01, a02, a04, a07, and a10, and 97-04 grains a02 and a04. The modeling space was specified as: 1200-0 Ma and 250-0°C. For the sake of demonstration and ease of plot visualization, the simulation was terminated when a modest number of 10 "acceptable" paths (green curves) were found at the 0.05 level. While these results certainly do not signify a robust pool of paths, the best-fit path is shown for discussion (black curve). A t-T path like the best-fit (i.e., beginning at low temperature) may not be wholly legitimate from a thermochronological perspective, as it leaves out some earlier part of the history in which daughter products would have been retained—but it does establish that the AHe dates can be reproduced with (re)heating only—and that any sensitivity to initial cooling in the Neoproterozoic would be lost due to heating in the Phanerozoic. Regional burial heating in the early-middle Paleozoic and late Mesozoic are both plausible, if not highly likely for this location (e.g., 17-23), and corroborated by the thermal history utilizing multi-system thermochronology in Figure 2 of the main text and the modeling shown in Figure S1 (also see Fig. S5). NOTES ON MODELING: We did not impose a Precambrian surface "exploration box" between 800–440 Ma at 0–40 $^{\circ}$ C, or a small 200–180 $^{\circ}$ C box from 1100–1000 Ma derived from regional 40 Ar/ 39 Ar K-feldspar data presented in McDannell et al. (11)—as these are either assumed conditions lacking a physical geological basis and/or have the potential to unduly influence the inversion due to the limited sensitivity of the input AHe data to high ($> 100^{\circ}$ C) and low ($< 50^{\circ}$ C) temperatures. Instead, a large t-T box was placed between 1200–480 Ma from 250–0°C. The constraint/exploration boxes were the same as Sturrock et al. (1) for the Phanerozoic, except the Ordovician "surface box" was extended to 40°C (less certain than locations near the Hudson Bay unconformity) and the upper temperature limit was set to 120° C for the larger boxes. Parameter settings for paths between boxes: segments halved 5 times and randomizer style was "gradual" with an imposed heating-cooling rate limit of 5° C/Myr. The modern surface temperature was set to $2 \pm 2^{\circ}$ C. All other HeFTy model settings were the defaults or the same as those in Sturrock et al. (1).

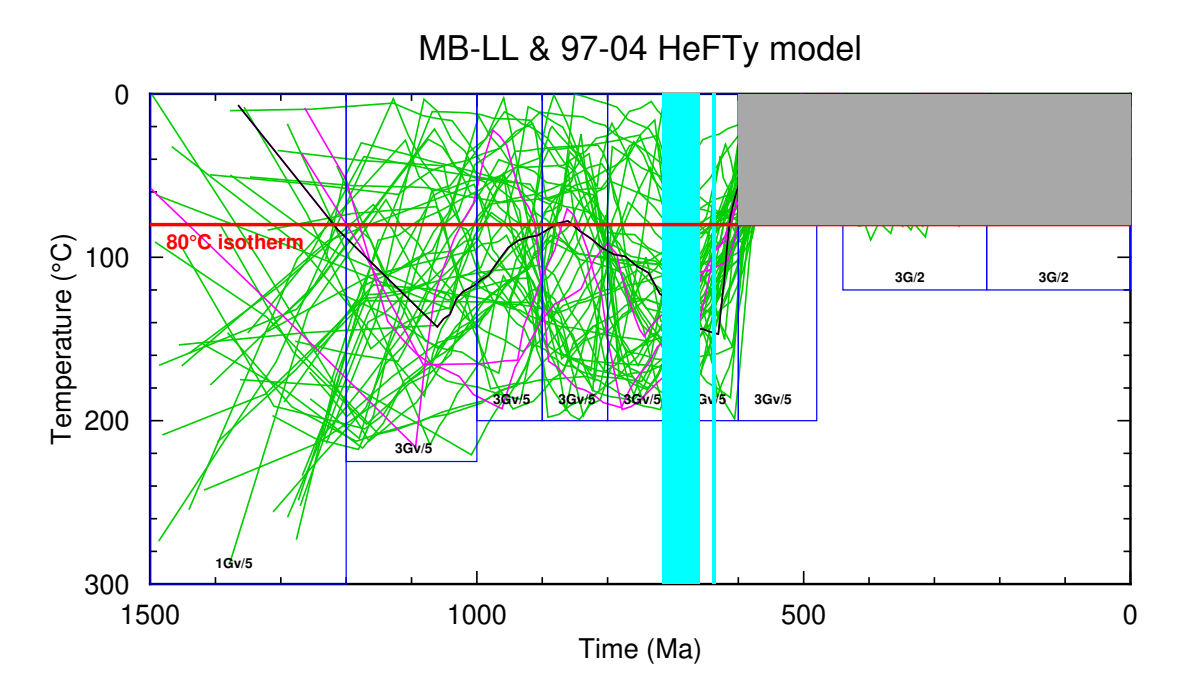


Fig. S3. Inversion of the Sturrock et al. (1) samples MB-LL and 97-04-7066 from the Trans-Hudson Orogen (their Fig. 4) using the HeFTy software v.1.9.3 (16). The same AHe grains were modeled as in Figure S2 under the same conditions but the model domain was expanded to: 1500-0 Ma and 300-0°C. The simulation was completed when 50 "acceptable" 0.05 solutions (green curves) were found (4 "good" magenta paths were also found at the 0.5 fit level). Increasing the number of exploration boxes can be an effective way to contend with the typically low number of $t\!-\!T$ points inherent to HeFTy Monte Carlo modeling. We used many boxes and increased path segmentation to boost the number of t-T nodes and provide more opportunities to find solutions (at the expense of computational speed) while modeling the grains with 10% errors. HeFTy is commonly run with the "monotonic consistent" setting that specifies history segments between boxes must be unidirectional. This setting has the potential to preferentially select for monotonic-cooling paths starting from high temperatures, since boxes are typically placed contextually as old = hot, and young = cold, thus always forcing cooling. Here we use the "monotonic variable" setting (16) for demonstration purposes. This option allows path segments between adjoining boxes to heat and/or cool, since the late Proterozoic interval is long and the geologic history is mostly unknown between > 1000 Ma to ca. 460 Ma and shows us where the observed data are well reproduced by a common subset of history segments that overlap in a relatively narrow region of t-T space (i.e., the thermal history envelope should collapse where t-T sensitivity/resolution are greatest). In HeFTy, this is dependent on many variables, such as the number of path segments allowed between exploration boxes (i.e., # t-T points), the heat-cooling rate, and the randomizer style (gradual/intermediate/episodic; refer to Ketcham (16)). The path segments and randomizer were set to 3 segments/gradual (3Gv/5) for all but the first large t-T box and the post-480 Ma history was set to 3 gradual segments (3G/2) with a heating-cooling rate limit for the Precambrian of 5° C/Myr and post-480 Ma rate of 2° C/Myr. The reduced allowable rate < 480 Ma prevented wild fluctuations in solutions. Importantly, the portion of the thermal history where there is clear AHe sensitivity (region shaded in gray) agrees well with the same portion of our multi-thermochronometer QTQt thermal history in Figure 2 of the main text (also see Fig. S5). Cyan bars are the Cryogenian glacial intervals.

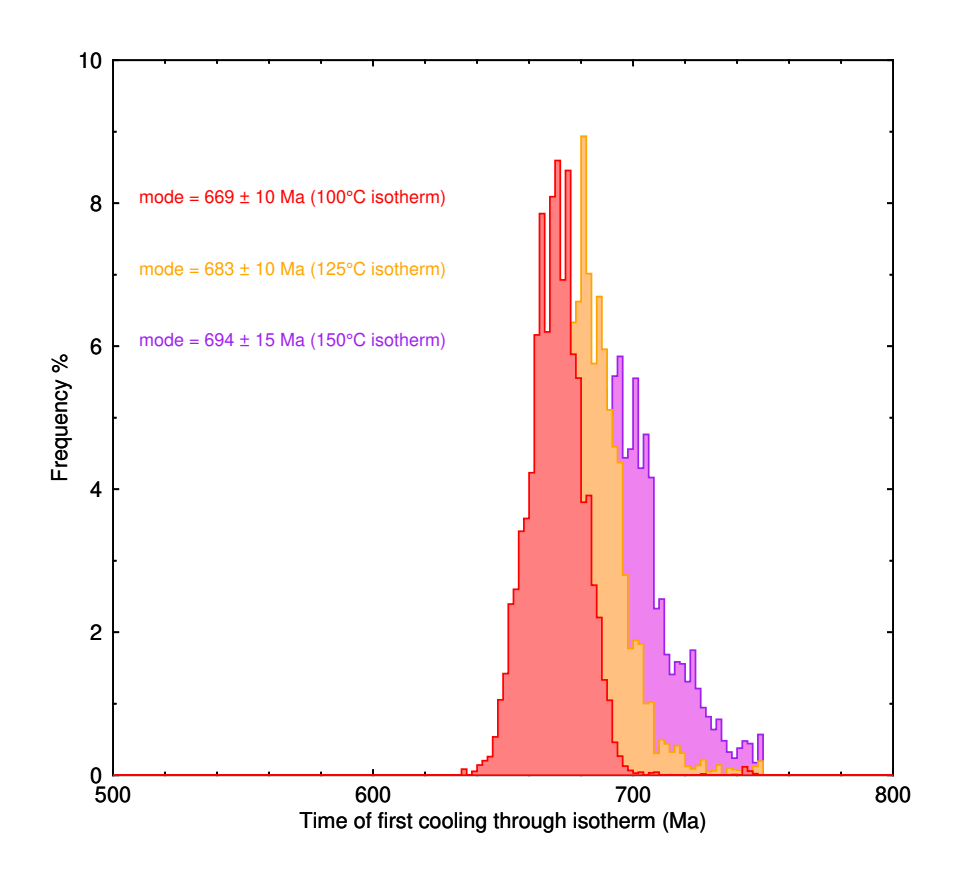


Fig. S4. Timing of first cooling through the 150° C, 125° C, and 100° C isotherms (window between 750–500 Ma) for the QTQt model results in Figure 2 of the main text (also see Fig. S5 below) shown as distributions drawn from the 500,000 post-burn-in t–T paths. We chose the half-maximum 100° C isotherm of the \sim 200° C of total Neoproterozoic cooling as representing peak cooling. Other cooling modes are shown for different isotherms for comparison, but regardless of isotherm chosen all of them exhibit cooling during Cryogenian glacial intervals. The high-temperature isotherms are offset earlier with respect to the slope of cooling (i.e., the cooling rate \sim 2° C/Myr). The half-maximum 100° C isotherm was chosen in the spirit of the spectroscopy and signal processing application of "full width at half-maximum" (FWHM) for providing the distance (width) between points on a curve or distribution at which half of the maximum value is reached—or when the independent variable is time, the adopted nomenclature is "full duration at half-maximum" (FDHM). The FDHM approximates when the first derivative of the cooling curve is maximized. Here, the FDHM = $669^{+1.0}_{-6}$ Ma at the 100° C isotherm for the W. Hudson Bay samples S481 and S499, and is in agreement with the mean $(670 \pm 10.4 \text{ Ma}; 1\sigma)$ and modal values (latter calculated using least median of squares method, i.e., the modal approximation and scale using the midpoint of the shortest half length of the data (24) in Generic Mapping Tools (GMT) 6.1.1 module *pshistogram* (25)). The 100° C isotherm is also preferred because the cooling path midpoint is less influenced by varying the number or position of t–t points in the accepted thermal histories (i.e., inflection point biases at higher temperatures or rate changes), or from nuances that may be introduced by thermochronologic data sensitivity/resolution. Note: the Athabasca QTQt inversion with applied geologic constraints published in McDannell et al. (10) shows

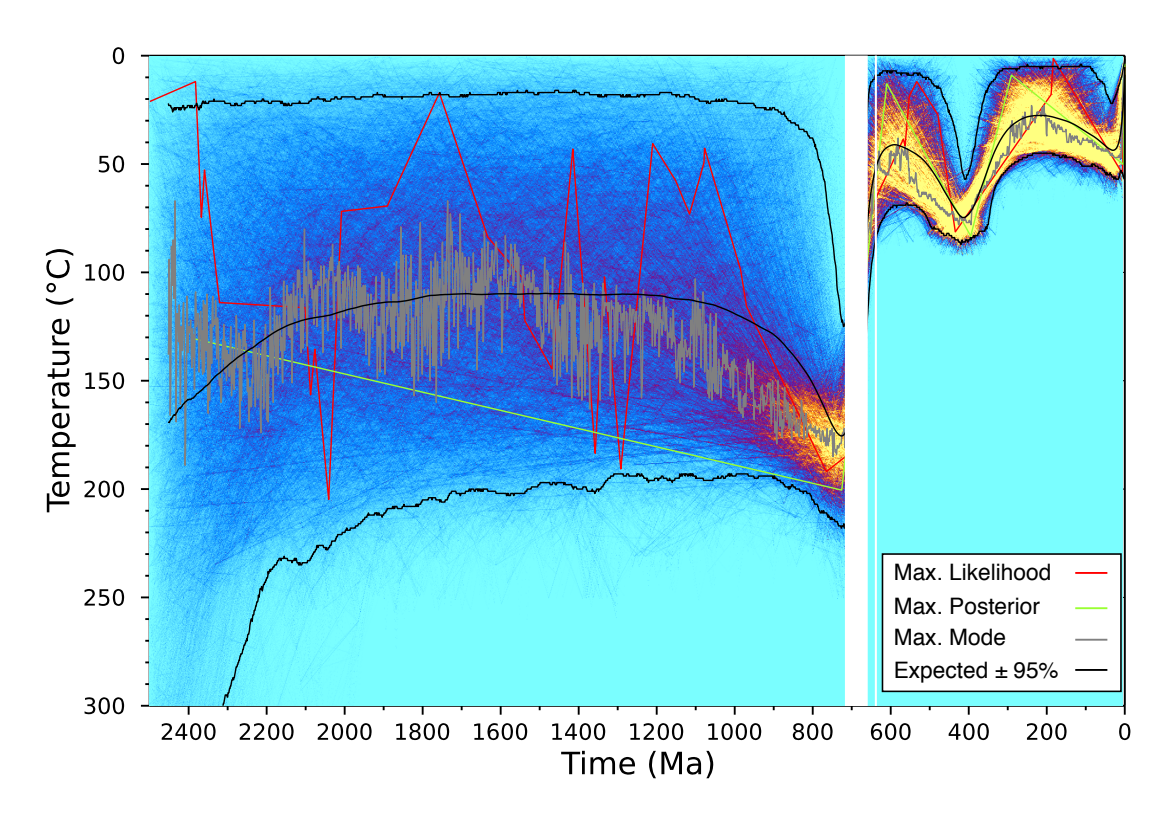


Fig. S5. QTQt inversion result from the main text (Figure 2) for samples 97-10-481 and 97-10-499 showing the individual t-T models discussed by Gallagher (26). We prefer to show all of the accepted model paths and the fits to the data as predicted date distributions. The maximum likelihood (best-fit model shown as red curve; usually the most complex with greatest number of t-T points), maximum posterior (green curve), which is the thermal history that has the maximum posterior probability, and is usually the simplest (fewest t-T points). The posterior probability combines the likelihoods and prior probabilities for each model, attempting to balance fitting the data with model complexity. The maximum mode solution (gray curve) is constructed at a 1 Myr interval by running along the peak of the marginal distribution, while the Expected model (black curve) is essentially the weighted mean of the marginal distribution (\pm 95% credible interval). The Mode and Expected paths are not solutions found during the inversion but are instead summaries of the t-T ensemble. Refer to Gallagher (26), Gallagher and Ketcham (27), and Gallagher and Ketcham (28) for more details on individual QTQt models and outputs. White shaded bars on the plot represent the Sturtian and Marinoan glaciations. We refrained from modeling the apatite U-Pb data in our primary model since QTQt explored the early (> 2400 Ma) ~400°C portion of the model independently, and the high-temperature metamorphic record does not greatly influence the late Proterozoic-Phanerozoic history. A separate model (not shown) with a 2466 \pm 68 Ma apatite U-Pb "t-T box" between 400–500° C showed similar results. Note: inverting the two AFT data sets together or individually does not change the t-T model results or our interpretations. In terms of model validation, the only robust geologic constraint for these samples is the basement nonconformity contact (< 5 km away) with the overlying middle Upper Ordovician Portage Chute Formation of the Bad Cache Rapids Group (W. Hudson Bay Basin) that is ca. 453-447.5 Ma in age (Maysvillian Stage), or ca. 470-450 Ma in age (29), depending on the outcrop location (30) and the applied age model (e.g., 29, 31, 32). In general, the Ordovician rocks in the Hudson Bay region are Edenian to Richmondian in age (ca. 454-444 Ma) (33-35), but are as old as ca. 475 Ma in the northerly Foxe Basin (36). Similarly, the nearby Williston Basin formed by the Cambrian and was undergoing rapid subsidence after ca. 488 Ma (or earlier) during deposition of the Deadwood Formation and the Middle Ordovician Winnipeg Formation (ca. 471-458 Ma depositional age; 37). Sturrock et al. (1, and refs. therein) quote a depositional age of 480-440 Ma for the Winnipeg Formation and a depositional age of 460-440 Ma for the Bad Cache Rapids Group. Considering the regional variability and age uncertainties, we prefer the most permissive age range for the regional deposition of Ordovician strata between ca. 480-440 Ma, or a locally less permissive age range of ca. 470-445 Ma for the Hudson Bay Basin. This requires the sampled basement to be at or near the surface before ca. 470-460 Ma. The QTQt maximum likelihood model t-T path displays a broad minimum from 552-479 Ma at reasonable paleo surface temperatures of ~12-27°C, followed by a maximum burial heating temperature of ~81°C at 434 Ma—in overall general agreement with the regional geology (38).

Table S1. Zircon (U-Th)/He data for samples 97-10-481 and 97-10-499, northern Manitoba, Hearne Domain, Canadian Shield

Sample*	± e	H	¹He	+	∟ lota	⊬	Th a	+	c	H	₹	H	e_	Length	Width 1	Width 2	Tip 1	Tip 2	Rs (Ft)	Ţ	Raw Date	1 SE	Corrected Date	10% error
	(ncc)	abs.	(atoms)	abs.	(atoms)	abs.	(atoms)	abs.	(ppm)		(ppm)		(ppm)	(mm)	(mm)	(mm)	(mm)	(mH)	(mm)		(Ma)	(Ma)	(Ma)	
97-10-481-z1	54.21	0.095	1.457E+12	2.555E+09	2.222E+12	6.077E+10	5.106E+11	2.196E+10	98.0	2.7	22.0	0.9	103	247.3	98.6	97.2	36.5	29.2	64.9	0.816	465.6	11.6	570.6	57
97-10-481-z2	40.28	0.039	1.082E+12	1.046E+09	1.685E+12	5.251E+10	9.757E+11	2.363E+10	160.4	5.0	90.6	2.2	182	434.8	128.8	113.0	48.3	44.3	51.6	0.769	425.8	11.3	553.7	55
97-10-481-z3	59.62	0.033	1.602E+12	8.750E+08	3.332E+12	1.192E+11	5.330E+11	1.681E+10	318.9	11.4	49.7	1.6	331	206.2	106.8	90.5	41.1	32.9	50.3	0.764	350.3	11.7	458.5	46
97-10-481-z4	72.05	0.112	1.936E+12	3.009E+09	4.218E+12	1.448E+11	4.068E+10	1.966E+09	546.2	18.8	5.1	0.2	547	285.6	126.1	123.4	54.0	44.1	47.5	0.750	345.9	11.5	461.2	46
97-10-481-z5	183.52	0.234	4.931E+12	6.278E+09	4.618E+13	2.165E+12	1.930E+11	1.067E+10	1014.2	47.6	4.1	0.2	1015	225.0	74.4	60.1	39.9	28.5	83.4	0.857	82.6	3.8	96.4	10
97-10-481-z6	36.25	0.031	9.739E+11	8.383E+08	1.240E+12	2.415E+10	4.557E+11	1.504E+10	149.0	2.9	53.4	1.8	162	154.0	77.8	76.7	26.6	26.5	48.7	0.758	538.3	9.2	710.1	71
97-10-481-z7	36.51	0.048	9.811E+11	1.283E+09	1.464E+12	3.244E+10	5.123E+11	1.361E+10	134.3	3.0	45.8	1.2	145	180.8	84.0	74.0	24.6	22.8	51.3	0.770	464.1	9.2	602.7	60
97-10-499-z1	0.27	0.001	7.329E+09	3.803E+07	7.144E+12	1.340E+11	1.261E+12	1.769E+10	996.4	18.7	171.5	2.4	1037	166.2	71.9	65.0	0.0	0.0	43.3	0.730	0.8	0.01	1	0.1
97-10-499-z2	1.13	0.004	3.034E+10	1.120E+08	1.715E+13	3.848E+11	1.577E+12	2.815E+10	1730.1	38.8	155.0	2.8	1767	185.4	76.2	76.0	0.0	0.0	48.2	0.758	1.4	0.03	1.8	0.2
97-10-499-z3	94.61	0.109	2.542E+12	2.931E+09	1.489E+13	3.775E+11	3.943E+12	8.463E+10	844.7	21.4	218.1	4.7	897	225.4	94.0	90.0	0.0	0.0	58.0	0.797	124.1	2.9	155.8	16
97-10-499-z4	5.10	0.008	1.370E+11	2.101E+08	4.061E+12	1.039E+11	3.728E+11	1.275E+10	808.6	20.7	72.4	2.5	826	143.5	106.3	81.1	35.9	34.7	40.8	0.710	25.7	0.6	36.2	4
97-10-499-z5	0.55	0.003	1.468E+10	8.912E+07	9.688E+12	2.911E+11	3.202E+12	9.143E+10	838.7	25.2	270.2	7.7	903	233.3	134.6	121.9	54.5	46.3	54.5	0.781	<u>:</u>	0.03	1.4	0.1

*Analyses performed at the University of Cagary by Dr. William Matthews using the methods of McKay et al. (39). Raw dates calculated in IsoplotR (40) from atoms of He, U, and Th. Alpha-loss (Ft) correction uses the grain length/width dimensions, where zircon tip lengths (if applicable) are measured from the tetragonal grain termination inward to pyramidal-prism tace boundary (41). Alpha-particle stopping distances are from Kelcham et al. (42) and "fts" is Frequivalent spherical grain radius. The 10% error is an applied total estimated uncertainty derived from typical reproducibility of the Fish Canyon Tuff (FCT) zircon age standard (e.g., 43–45). FCT ircons were analysed in three appraise assessions and yielded a weighted mean Fi-corrected age of 28.9 ± 0.5 Ma (2-, n = 18/19). The assumed reference age for FCT ignimbrite emplacement is 28.2 Ma (46, 47, and refs. therein). The high-precision U-Pb age is 28.48 ± 0.06 Ma (2-) (48) and the ^{4.0} Ar sanidine age is 28.04 ± 0.18 Ma (2-) (49).

Table S2. Apatite (U-Th)/He data for sample 97-10-481, northern Manitoba, Hearne Domain, Canadian Shield

$\pm 2\sigma$ (Ma)	34	25	15	18	18
Corr. Date	328	387	398	315	264
Œ	0.646	0.540	0.589	0.661	0.625
⊕ (Ma)	10.5	14.9	4.4	5.8	5.6
Raw Date	215.4	214.2	238.2	210.7	167.2
⊕ (gn)	0.001	0.001	0.001	0.001	0.001
ES.	0.0290	0.0258	0.0870	0.0688	0.0475
# (gu)	0.001	0.001	0.004	0.002	0.001
Ę	0.0175	0.0121	0.1397	0.1015	0.0509
⊕ (gn)	0.001	0.001	0.002	0.003	0.001
-	0.0121	0.0072	0.0720	0.0681	0.0217
(ncc) +	0.002	0.003	0.013	0.008	0.004
⁴ He (ppm)	0.436	0.270	3.099	2.396	0.698
en	12	15	110	75	54
+ (mdd)	1.00	1.46	1.46	1.16	0.64
ES.	21.43	39.06	91.17	56.26	33.22
⊕ (mdd)	0.69	0.88	3.96	1.38	0.83
Ę	12.93	18.29	146.40	83.00	35.59
(bbm) +	0.58	1.08	1.84	2.12	0.78
5	8.91	10.92	75.53	55.66	15.15
\pm (nmol/g)	0.070	0.180	0.606	0.297	0.135
∓	14.339	18.264	144.933	87.426	21.752
Rs (mm)	38.9	29.1	35.0	41.7	38.0
width 2 (µm)	102.6	61.3	60.2	89.5	74.6
length 2 (µm)	80.3	64.2	148.5	131.7	125.4
width 1 (µm)	0.99	94.2	66.4	78.8	60.3
length 1 (µm)	73.3	64.2	145.6	117.5	134.0
Sample*	S481_a02	S418_a03	S418_a05	S418_a06	S418_a07

*Grain picked and analysed by Dr. James Metcalf at the University of Colorado-Boulder using the methods discussed in Sturrock et al. (1); grain terminations = 0, 0, 2, 2, 0, respectively. The quoted 2 σ uncertainty is total analytical error. Shards of Durango fluorapatite run in conjunction with these grains yield a date of 31.2 \pm 0.9 Ma (n = 9). The established reference age for Durango apatite is 31.44 \pm 0.18 Ma (2 σ) (50). Note: the AHe data were modeled with the Ketcham et al. (51) annealing algorithm.

Table S3. Apatite fission-track data for samples 97-10-481 and 97-10-499, northern Manitoba, Hearne Domain, Canadian Shield.

N_s	Area	²³⁸ U/ ⁴³ Ca	1 σ	$P_i\Omega_i$	$\sigma P_i^2 \Omega_i^2$	AFT age	1σ	\mathbf{D}_{par}	F	CI	ОН	1999 r _{mr0} †	eCl	U-Pb Date	2σ
	(cm^2)	(dmnls)	(dmnls)			(Ma)	(Ma)	(µm)	(apfu)	(apfu)	(apfu)	(dmnls)	(apfu)	(Ma)	(Ma)
34	2.91E-05	2.81E-02	7.42E-04	8.18E-07	4.66E-16	335	58	1.93	1.71	0.00	0.29	0.847	-0.020	2602	316
101	2.72E-05	8.28E-02	2.21E-03	2.25E-06	3.62E-15	361	38	1.84	1.70	0.00	0.30	0.849	-0.027	2399	366
71	2.91E-05	5.36E-02	1.26E-03	1.56E-06	1.35E-15	366	45	1.96	1.80	0.01	0.19	0.855	-0.044	2788	714
80	2.91E-05	5.95E-02	1.88E-03	1.73E-06	2.99E-15	371	44	1.78	1.84	0.00	0.16	0.857	-0.052	2435	370
77	2.43E-05	6.64E-02	2.12E-03	1.61E-06	2.64E-15	383	46	1.88	1.62	0.00	0.38	0.844	-0.012	_	_
55	2.33E-05	4.64E-02	1.15E-03	1.08E-06	7.19E-16	408	56	2.05	-	-	_	_	_	_	_
80	3.88E-05	3.95E-02	1.14E-03	1.53E-06	1.95E-15	418	49	1.50	1.75	0.00	0.24	0.844	-0.011	2448	504
132	3.88E-05	6.18E-02	1.41E-03	2.40E-06	3.00E-15	440	40	1.37	1.76	0.00	0.23	0.854	-0.042	2436	378
61	2.43E-05	4.52E-02	1.08E-03	1.10E-06	6.91E-16	445	58	1.56	1.64	0.00	0.36	0.848	-0.023	2518	342
77	2.18E-05	6.29E-02	1.34E-03	1.37E-06	8.55E-16	447	52	1.66	1.66	0.01	0.33	0.848	-0.024	2546	264
118	4.85E-05	4.28E-02	9.99E-04	2.08E-06	2.35E-15	453	44	1.83	1.64	0.00	0.36	0.842	-0.005	2457	426
54	1.75E-05	4.66E-02	1.16E-03	8.14E-07	4.08E-16	527	73	1.68	1.72	0.00	0.28	0.849	-0.028	2553	545
200	3.40E-05	8.81E-02	2.09E-03	2.99E-06	5.04E-15	530	41	1.81	1.73	0.01	0.27	0.847	-0.022	2517	250
76	2.91E-05	3.59E-02	8.79E-04	1.05E-06	6.55E-16	575	68	1.67	1.70	0.00	0.29	0.848	-0.025	2463	418
118	2.91E-05	5.55E-02	1.78E-03	1.62E-06	2.67E-15	577	57	1.77	1.66	0.00	0.34	0.844	-0.011	2470	476
78	2.91E-05	3.45E-02	8.89E-04	1.01E-06	6.70E-16	612	72	1.65	1.66	0.01	0.33	0.842	-0.005	2658	534
53	2.62E-05	2.55E-02	7.29E-04	6.69E-07	3.65E-16	624	88	1.65	1.76	0.00	0.24	0.847	-0.020	2484	601
334	4.85E-05	8.53E-02	1.99E-03	4.14E-06	9.28E-15	635	39	1.43	1.75	0.00	0.25	0.852	-0.037	2413	265
164	2.91E-05	6.81E-02	1.84E-03	1.98E-06	2.88E-15	650	55	1.70	1.74	0.00	0.25	0.852	-0.036	2374	452
92	4.85E-05	2.18E-02	6.01E-04	1.06E-06	8.50E-16	683	75	1.80	1.72	0.00	0.28	0.844	-0.012	2522	683
98	4.85E-05	2.13E-02	5.93E-04	1.03E-06	8.28E-16	740	79	1.54	1.68	0.00	0.32	0.844	-0.011	2543	709
69	2.43E-05	2.81E-02	7.43E-04	6.83E-07	3.25E-16	786	98	1.69	1.62	0.01	0.37	0.844	-0.011	2510	571
85	2.91E-05	2.86E-02	7.57E-04	8.32E-07	4.86E-16	794	90	2.08	1.71	0.00	0.29	0.847	-0.019	2750	527
61	3.88E-05	1.52E-02	4.75E-04	5.89E-07	3.40E-16	805	107	1.70	1.63	0.00	0.37	0.847	-0.021	2682	825
72	4.85E-05	1.42E-02	4.54E-04	6.88E-07	4.86E-16	813	100	1.85	1.71	0.00	0.29	0.851	-0.034	2460	629
96	3.11E-05	2.94E-02	8.01E-04	9.14E-07	6.19E-16	815	87	1.79	1.92	0.00	0.08	0.855	-0.045	2581	515
73	4.85E-05	1.08E-02	3.20E-04	5.26E-07	2.41E-16	1056	129	1.79	1.56	0.02	0.42	0.839	0.005	2629	948
2609	8.95E-04			3.81E-05	4.68E-14	543	14	1.74	1.71	0.00	0.29	0.847	-0.023	2505	83
97-10-481	0.002 0 1			0.0.2.00		554	32						0.020	2524	56
	4005.05	0.005.00	4 705 00	0.445.00	0.005.45		-				0.50	2.004			
142	4.66E-05	6.69E-02	1.79E-03	3.11E-06	6.99E-15	367	33	1.94	1.47	0.01	0.52	0.834	0.019	2309	447
162	5.82E-05	4.87E-02	2.27E-03	2.84E-06	1.75E-14	456	42	2.22	1.51	0.00	0.48	0.836	0.012	2370	718
328	6.79E-05	8.03E-02	3.54E-03	5.46E-06	5.79E-14	479	35	2.06	1.52	0.01	0.47	0.827	0.038	2457	678
686	6.79E-05	1.66E-01	3.82E-03	1.13E-05	6.74E-14	485	23	1.88	1.40	0.01	0.59	0.812	0.078	2372	279
75	2.91E-05	4.16E-02	1.28E-03	1.21E-06	1.40E-15	493	60	1.70	1.56	0.00	0.44	0.838	0.007	2296	485
89	2.91E-05	4.83E-02	1.32E-03	1.41E-06	1.48E-15	503	56	1.94	1.45	0.00	0.55	0.832	0.023	2344	401
199	4.85E-05	6.22E-02	1.58E-03	3.02E-06	5.84E-15	523	40	1.83	1.45	0.00	0.54	0.826	0.041	2385	347
224	5.82E-05	5.68E-02	3.09E-03	3.31E-06	3.23E-14	537	47	1.90	1.45	0.01	0.54	0.827	0.039		
55	3.40E-05	2.32E-02	5.96E-04	7.87E-07	4.11E-16	554	77	1.80	1.50	0.01	0.49	0.837	0.009	2343	515
55	2.72E-05	2.82E-02	8.64E-04	7.67E-07	5.52E-16	567	79	1.99	1.52	0.00	0.48	0.832	0.024	2478	757
321	4.37E-05	9.92E-02	5.86E-03	4.33E-06	6.55E-14	585	49	2.38	1.52	0.00	0.48	0.827	0.037	2392	998
340	6.79E-05	6.66E-02	3.86E-03	4.53E-06	6.89E-14	593	48	1.77	1.49	0.00	0.51	0.829	0.034	_	_
157	3.88E-05	5.19E-02	1.32E-03	2.02E-06	2.65E-15	614	52	1.93	1.63	0.00	0.37	0.843	-0.008	2236	361
422	5.82E-05	9.01E-02	3.09E-03	5.24E-06	3.25E-14	633	39	1.99	1.60	0.00	0.39	0.842	-0.006	-	-
97	3.88E-05	3.06E-02	1.62E-03	1.19E-06	3.97E-15	643	75	1.94	1.46	0.00	0.54	0.825	0.043	2512	926
181	3.88E-05	5.53E-02	1.61E-03	2.15E-06	3.91E-15	662	54	1.97	1.48	0.01	0.52	0.828	0.034	2586	757
134	4.85E-05	3.07E-02	1.13E-03	1.49E-06	3.02E-15	704	67	1.89	1.54	0.01	0.45	0.836	0.013	2576	659
306	4.85E-05	6.74E-02	1.74E-03	3.27E-06	7.16E-15	731	48	1.98	1.42	0.00	0.57	0.821	0.054	2599	444
363	6.79E-05	5.55E-02	3.98E-03	3.77E-06	7.31E-14	751	68	1.79	1.45	0.00	0.55	0.830	0.030	2501	1053
398	6.79E-05	6.06E-02	3.66E-03	4.11E-06	6.18E-14	754	61	1.92	1.56	0.00	0.44	0.820	0.057	_	-
	0.005.04			6.53E-05	5.14E-13	574	14	1.94	1.50	0.00	0.50	0.829	0.029	2384	121
4734	9.86E-04			0.55E-05	0.142 10	0, -		1.04		0.00	0.50	0.020	0.023	2004	

 ${
m N_S}$ = spontaneous track count; ${
m P}_i$ = ablation pit depth-weighted $^{238}{
m U}/^{43}{
m Ca}$ ratio; Ω_i = track count area; dmnls = dimensionless units

AFT single-grain ages are calculated using the LA-ICPMS (ζ -calibration) method with modified ζ = 8.2727, standard error (ζ) = 0.1407 and z^{28} U total decay constant of 1.55125 \times 10 z^{-10} yr z^{-1} . Upper panel is S481 and lower panel is S499. Bottom table row (bold) displays the analysis sums, AFT pooled/central age \pm 1 σ error (light/dark gray shading, respectively), and the mean values for the tabulated elements/kinetic parameters D $_{par}$, F, Ci, OH, r $_{mr0}$ (median), and effective CI (eCI; (6, 9)). Individual grain D $_{par}$ values are the mean of 4 measurements and r $_{mr0}$ and eCl are calculated from Carlson et al. (52) equations \uparrow .

AFT central age for S481: age dispersion = 28%, $P(\chi^2)$ = 0.00; AFT central age for S499 age dispersion = 16%, $P(\chi^2)$ = 0.00.

Samples fall χ^2 test due to high N analyses and higher age precision (e.g., 53–56) compared to the AFT external detector method (57). Combined sample central age: 563 ± 21 Ma (1σ).

Individual apatite U-Pb dates are common Pb-corrected isotopic sums. Summary U-Pb date reported is the simple weighted mean of individual dates $\text{S481: } 2505 \pm 83 \text{ Ma; } 2\sigma, \text{n} = 25/25, \text{MSWD} = 0.18, \text{P}(\chi^2) = 1.00; \text{S499: } 2384 \pm 121 \text{ Ma; } 2\sigma, \text{n} = 16/16, \text{MSWD} = 0.19, \text{P}(\chi^2) = 1.00.$

The weighted mean 207 Pb/ 206 Pb date was calculated in IsoplotR (40) using Stacey and Kramers (58) common-Pb correction and 238 U/ 206 Pb and 207 Pb/ 206 Pb isotopic ratios S481: 2524 \pm 56 Ma; 2 σ , n = 25/25, MSWD = 0.5, P(χ^2) = 1.00; S499: 2434 \pm 74 Ma; 2 σ , n = 16/16, MSWD = 0.6, P(χ^2) = 0.9.

Laser ablation fission-track analyses (LAFT) performed by Dr. Paul B. O'Sullivan (GeoSep Services). Electron probe microanalysis (EPMA) data were analysed at Washington State University Peter Hooper GeoAnalytical Laboratory by Dr. Scott Boroughs. Refer to recent overviews of LAFT-EPMA analytical protocols in McDannell et al. (5), McDannell et al. (59), Complete EPMA data available upon reasonable request.

Table S4. Sample 97-10-481 fission-track length measurements with kinetic parameters

Length (μm)	c-angle	\mathbf{D}_{par} ($\mu\mathbf{m}$)	\mathbf{D}_{per} ($\mu\mathbf{m}$)	Cl (apfu)	OH (apfu)	\mathbf{r}_{mr0}	eCl (apfu)
13.90	59.19	1.68	0.27	0.002	0.267	0.848	-0.025
12.73	78.45	1.62	0.30	0.004	0.110	0.859	-0.058
13.98	11.98	1.62	0.30	0.004	0.110	0.859	-0.058
12.75	68.73	1.62	0.30	0.004	0.110	0.859	-0.058
13.77	41.21	1.62	0.30	0.004	0.110	0.859	-0.058
15.93	35.05	1.63	0.28	0.003	0.217	0.853	-0.040
13.99	45.08	1.63	0.28	0.003	0.217	0.853	-0.040
15.41	41.42	1.63	0.28	0.003	0.217	0.853	-0.040
13.23	30.04	1.63	0.28	0.003	0.217	0.853	-0.040
12.04	53.90	1.63	0.28	0.003	0.217	0.853	-0.040
13.01	62.06	1.63	0.28	0.003	0.217	0.853	-0.040
10.94	70.21	1.63	0.28	0.003	0.217	0.853	-0.040
13.91	8.34	1.63	0.28	0.003	0.217	0.853	-0.040
9.22	57.83	1.83	0.32	0.002	0.381	0.845	-0.016
12.16	54.56	1.83	0.32	0.002	0.381	0.845	-0.016
10.30	57.51	1.83	0.32	0.002	0.381	0.845	-0.016
13.77	29.19	1.53	0.27	0.009	0.376	0.840	0.000
12.74	57.74	1.53	0.27	0.009	0.376	0.840	0.000
13.83	42.92	1.57	0.30	0.007	0.299	0.849	-0.026
12.59	52.86	1.57	0.30	0.007	0.299	0.849	-0.026
12.38	35.99	1.57	0.30	0.007	0.299	0.849	-0.026
13.85	24.11	1.57	0.30	0.007	0.299	0.849	-0.026
12.27	71.90	1.57	0.30	0.007	0.299	0.849	-0.026
14.18	39.79	1.57	0.30	0.007	0.299	0.849	-0.026
14.66	34.66	1.57	0.30	0.007	0.299	0.849	-0.026
15.14	36.45	1.57	0.30	0.007	0.299	0.849	-0.026
13.86	23.42	1.86	0.31	0.000	0.210	0.847	-0.021
10.78	69.55	1.86	0.31	0.000	0.210	0.847	-0.021
14.45	32.70	1.86	0.31	0.000	0.210	0.847	-0.021
14.77	51.35	1.86	0.31	0.000	0.210	0.847	-0.021
14.66	30.84	$1.61 \\ 1.61$	$0.27 \\ 0.27$	$0.003 \\ 0.003$	$0.277 \\ 0.277$	$0.851 \\ 0.851$	-0.032
13.07 10.93	80.11 33.58	1.61	$0.27 \\ 0.27$	0.003	0.277	0.851	-0.032 -0.032
8.81	33.38 47.83	1.76	0.27 0.32	0.003 0.002	0.241	0.851	-0.032
13.08	48.42	1.76	0.32 0.32	0.002	0.241 0.241	0.851	-0.033
10.10	49.30	1.76	0.32	0.002	0.241 0.241	0.851	-0.033
14.01	67.12	1.79	0.32	0.002 0.004	0.328	0.844	-0.011
11.61	64.42	1.79	0.40	0.004	0.328	0.844	-0.011
15.57	65.81	1.79	0.40	0.004	0.328	0.844	-0.011
13.64	36.97	1.79	0.40	0.004	0.328	0.844	-0.011
13.44	33.56	1.79	0.40	0.004	0.328	0.844	-0.011
14.09	38.69	1.79	0.40	0.004	0.328	0.844	-0.011
9.28	60.32	1.79	0.40	0.004	0.328	0.844	-0.011
11.80	71.02	1.90	0.36	0.000	0.222	0.848	-0.023
9.00	82.76	1.90	0.36	0.000	0.222	0.848	-0.023
11.43	61.81	1.90	0.36	0.000	0.222	0.848	-0.023
12.82	60.00	1.90	0.36	0.000	0.222	0.848	-0.023
11.75	67.70	1.90	0.36	0.000	0.222	0.848	-0.023
9.24	68.62	1.67	0.30	0.002	0.158	0.855	-0.047
13.44	48.75	1.67	0.30	0.002	0.158	0.855	-0.047
13.38	61.44	1.67	0.30	0.002	0.158	0.855	-0.047
11.82	65.29	1.67	0.30	0.002	0.158	0.855	-0.047
10.80	62.88	1.67	0.30	0.002	0.158	0.855	-0.047
9.28	54.84	1.91	0.31	0.003	0.236	0.852	-0.036
14.09	46.25	1.91	0.31	0.003	0.236	0.852	-0.036
9.32	82.01	1.91	0.31	0.003	0.236	0.852	-0.036
15.29	39.31	1.91	0.31	0.003	0.236	0.852	-0.036
13.76	43.69	1.91	0.31	0.003	0.236	0.852	-0.036
8.25	67.71	1.91	0.31	0.003	0.236	0.852	-0.036

7D 11	α		C	•	
Table	54	continued	trom	previous	page

Longeth (um)	a amala			On previous			oCl (onfu)
Length $(\mu \mathbf{m})$	c-angle	\mathbf{D}_{par} ($\mu\mathbf{m}$)	\mathbf{D}_{per} ($\mu\mathbf{m}$)	Cl (apfu)	OH (apfu)	\mathbf{r}_{mr0}	eCl (apfu)
10.48	65.17	1.91	0.31	0.003	0.236	0.852	-0.036
15.61	52.59	1.91	0.31	0.003	0.236	0.852	-0.036
11.15	77.35	1.73	0.33	0.009	0.162	0.849	-0.026
11.12	43.79	1.73	0.33	0.009	0.162	0.849	-0.026
13.03	61.55	1.73	0.33	0.009	0.162	0.849	-0.026
13.73	54.02	1.73	0.33	0.009	0.162	0.849	-0.026
12.53	57.51	1.99	0.34	0.002	0.314	0.843	-0.009
9.44	73.48	1.99	0.34	0.002	0.314	0.843	-0.009
11.78	51.56	1.99	0.34	0.002	0.314	0.843	-0.009
12.82	49.56	1.77	0.32	0.006	0.438	0.843	-0.007
8.84	39.55	1.77	0.32	0.006	0.438	0.843	-0.007
12.46	32.54	1.77	0.32	0.006	0.438	0.843	-0.007
12.71	62.58	1.77	0.32	0.006	0.438	0.843	-0.007
13.34	61.18	1.77	0.32	0.006	0.438	0.843	-0.007
13.95	79.42	1.77	0.32	0.006	0.438	0.843	-0.007
12.96	53.90	1.77	0.32	0.006	0.438	0.843	-0.007
15.33	35.62	1.77	0.32	0.006	0.438	0.843	-0.007
		1.69	0.32 0.41	0.000	0.458 0.255		
11.29	$60.55 \\ 51.74$					0.851	-0.032
13.85		1.69	0.41	0.000	0.255	0.851	-0.032
9.24	55.19	1.69	0.41	0.000	0.255	0.851	-0.032
12.18	65.17	1.70	0.30	0.004	0.320	0.848	-0.025
12.00	61.92	1.70	0.30	0.004	0.320	0.848	-0.025
11.80	39.13	1.70	0.30	0.004	0.320	0.848	-0.025
10.20	74.51	1.70	0.30	0.004	0.320	0.848	-0.025
11.72	29.57	1.43	0.29	0.002	0.259	0.853	-0.038
12.55	52.25	1.43	0.29	0.002	0.259	0.853	-0.038
11.37	77.23	1.43	0.29	0.002	0.259	0.853	-0.038
13.00	31.15	1.48	0.35	0.007	0.248	0.852	-0.036
13.62	56.22	1.80	0.44	0.003	0.326	0.836	0.011
13.41	60.92	1.80	0.44	0.003	0.326	0.836	0.011
11.65	46.33	1.80	0.44	0.003	0.326	0.836	0.011
16.12	6.41	1.80	0.44	0.003	0.326	0.836	0.011
13.10	34.85	1.80	0.44	0.003	0.326	0.836	0.011
11.78	55.89	1.98	0.30	0.000	0.288	0.850	-0.029
10.96	28.00	1.98	0.30	0.000	0.288	0.850	-0.029
9.72	55.24	1.98	0.30	0.000	0.288	0.850	-0.029
11.50	63.91	1.46	0.26	0.000	0.264	0.853	-0.039
11.26	52.09	1.46	0.26	0.000	0.264	0.853	-0.039
11.67	64.46	1.46	0.26	0.000	0.264	0.853	-0.039
14.16	63.88	1.46	0.26	0.000	0.264	0.853	-0.039
12.52	54.05	1.46	0.26	0.000	0.264	0.853	-0.039
11.74	60.95	1.79	0.23	0.009	0.272	0.840	0.000
9.65	54.92	1.79	0.23	0.009	0.272	0.840	0.000
11.26	68.57	1.79	0.23	0.009	0.272	0.840	0.000
11.08	39.89	1.79	0.23	0.009	0.272	0.840	0.000
			0.26				
12.76	34.50	1.61		0.000	0.185	0.854	-0.044
13.71	22.82	1.61	0.26	0.000	0.185	0.854	-0.044
15.76	38.25	1.55	0.30	0.004	0.344	0.849	-0.026
11.18	63.21	1.55	0.30	0.004	0.344	0.849	-0.026
11.23	56.88	1.55	0.30	0.004	0.344	0.849	-0.026
12.46	61.49	1.55	0.30	0.004	0.344	0.849	-0.026
15.43	48.73	1.76	0.36	0.002	0.193	0.838	0.006
12.16	68.41	1.76	0.36	0.002	0.193	0.838	0.006
13.18	64.22	1.76	0.36	0.002	0.193	0.838	0.006
13.90	56.02	1.76	0.36	0.002	0.193	0.838	0.006
13.11	52.86	1.74	0.32	0.000	0.292	0.841	-0.001
12.87	60.22	1.74	0.32	0.000	0.292	0.841	-0.001
14.68	44.23	1.84	0.32	0.000	0.374	0.840	0.000
11.85	44.28	1.84	0.32	0.000	0.374	0.840	0.000

Table S4 continued from previous page

Length $(\mu \mathbf{m})$	c-angle	\mathbf{D}_{par} ($\mu\mathbf{m}$)	\mathbf{D}_{per} ($\mu\mathbf{m}$)	Cl (apfu)	OH (apfu)	\mathbf{r}_{mr0}	eCl (apfu)
12.86	41.52	1.84	0.32	0.000	0.374	0.840	0.000
9.02	54.24	1.94	0.57	0.000	0.273	0.847	-0.020
11.53	43.15	1.94	0.57	0.000	0.273	0.847	-0.020
14.68	25.15	1.68	0.25	0.005	0.313	0.838	0.007
12.86	33.60	1.68	0.25	0.005	0.313	0.838	0.007
13.52	58.98	1.68	0.25	0.005	0.313	0.838	0.007
11.26	52.55	1.68	0.25	0.005	0.313	0.838	0.007
11.32	53.61	1.68	0.25	0.005	0.313	0.838	0.007
13.63	41.17	1.43	0.29	0.005	0.290	0.840	0.001
12.01	55.71	1.78	0.36	0.004	0.266	0.841	-0.003
9.96	38.19	1.78	0.36	0.004	0.266	0.841	-0.003
10.73	64.70	1.78	0.36	0.004	0.266	0.841	-0.003
10.46	87.98	1.78	0.36	0.004	0.266	0.841	-0.003

MTL = 12.43 \pm 1.77 μ m (1 σ , n = 131) \pm 0.16 std. error. Skewness = -0.212; Kurtosis = -0.529. Mean D_{par} = 1.72 (4 etch figures each measurement); mean D_{per} = 0.32; analyst: POS.

Table S5. Sample 97-10-499 fission-track length measurements with kinetic parameters

Length $(\mu \mathbf{m})$	c-angle	\mathbf{D}_{par} ($\mu\mathbf{m}$)	\mathbf{D}_{per} ($\mu\mathbf{m}$)	Cl (apfu)	OH (apfu)	\mathbf{r}_{mr0}	eCl (apfu)
11.91	68.16	1.95	0.30	0.007	0.436	0.834	0.019
12.54	64.33	1.95	0.30	0.007	0.436	0.834	0.019
11.80	78.45	1.95	0.30	0.007	0.436	0.834	0.019
13.44	72.87	1.95	0.30	0.007	0.436	0.834	0.019
12.18	70.86	1.95	0.30	0.007	0.436	0.834	0.019
9.20	58.09	1.95	0.30	0.007	0.436	0.834	0.019
10.92	52.40	1.95	0.30	0.007	0.436	0.834	0.019
10.20	74.43	1.95	0.30	0.007	0.436	0.834	0.019
12.94	38.65	1.95	0.30	0.007	0.436	0.834	0.019
10.58	60.17	1.95	0.30	0.007	0.436	0.834	0.019
13.06	23.59	1.95	0.30	0.007	0.436	0.834	0.019
13.70	55.43	1.95	0.30	0.007	0.436	0.834	0.019
9.73	78.37	1.95	0.30	0.007	0.436	0.834	0.019
12.81	42.08	1.95	0.30	0.007	0.436	0.834	0.019
9.90	77.09	1.95	0.30	0.007	0.436	0.834	0.019
10.67	73.51	1.95	0.30	0.007	0.436	0.834	0.019
13.15	59.45	1.95	0.30	0.007	0.436	0.834	0.019
11.33	58.74	1.95	0.30	0.007	0.436	0.834	0.019
12.45	61.62	1.95	0.30	0.007	0.436	0.834	0.019
13.38	26.77	1.95	0.30	0.007	0.436	0.834	0.019
10.79	73.36	1.95	0.30	0.007	0.436	0.834	0.019
12.06	60.01	1.95	0.30	0.007	0.436	0.834	0.019
12.05	48.16	1.95	0.30	0.007	0.436	0.834	0.019
12.23	60.64	1.95	0.30	0.007	0.436	0.834	0.019
9.62	70.09	1.95	0.30	0.007	0.436	0.834	0.019
12.92	71.88	1.95	0.30	0.007	0.436	0.834	0.019
12.61	75.28	1.75	0.30	0.007	0.531	0.823	0.048
14.27	68.72	1.75	0.30	0.007	0.531	0.823	0.048
12.76	30.85	1.75	0.30	0.007	0.531	0.823	0.048
9.26	36.85	1.75	0.30	0.007	0.531	0.823	0.048
9.84	60.10	1.75	0.30	0.007	0.531	0.823	0.048
9.95	79.79	1.75	0.30	0.007	0.531	0.823	0.048
10.71	76.28	1.75	0.30	0.005	0.492	0.833	0.020
12.10	50.81	1.75	0.30	0.005	0.492	0.833	0.020
13.38	34.28	1.75	0.30	0.005	0.492	0.833	0.020
13.38	29.94	1.75	0.30	0.005	0.492	0.833	0.020
12.32	53.07	1.75	0.30	0.005	0.492	0.833	0.020
11.71	68.37	1.86	0.25	0.006	0.461	0.829	0.033
8.68	74.51	1.86	0.25	0.006	0.461	0.829	0.033
13.33	73.42	1.86	0.25	0.006	0.461	0.829	0.033
10.17	68.52	1.86	0.25	0.006	0.461	0.829	0.033
12.88	55.31	1.86	0.25	0.006	0.461	0.829	0.033
13.32	69.12	1.86	0.25	0.006	0.461	0.829	0.033
11.31	50.90	1.86	0.25	0.006	0.461	0.829	0.033
12.37	52.77	1.86	0.25	0.006	0.461	0.829	0.033
14.70	17.91	1.81	0.28	0.004	0.440	0.827	0.037
12.85	77.08	1.85	0.31	0.000	0.376	0.837	0.010
9.24	54.91	1.85	0.31	0.000	0.376	0.837	0.010
10.94	53.00	1.85	0.31	0.000	0.376	0.837	0.010
12.69	44.73	1.99	0.28	0.006	0.468	0.822	0.052
11.75	82.90	1.99	0.28	0.006	0.468	0.822	0.052
13.72	70.42	1.99	0.28	0.006	0.468	0.822	0.052
13.09	63.72	1.99	0.28	0.006	0.468	0.822	0.052
13.78	47.95	1.99	0.28	0.006	0.468	0.822	0.052 0.052
12.45	39.95	1.99	0.28	0.006	0.468	0.822	0.052 0.052
10.24	43.32	1.99	0.28	0.006	0.468	0.822	0.052
11.81	78.01	$\frac{1.99}{2.12}$	0.25	0.005	0.511	0.832	0.032 0.024
10.17	59.85	$\frac{2.12}{2.12}$	0.25	0.005	0.511	0.832	0.024
11.73	50.86	$\frac{2.12}{2.12}$	0.25	0.005	0.511	0.832	0.024
11.10	50.00	4.14	0.20	0.000	0.011	0.002	0.024

TO 11 OF		c	•	
Table 55	continued	trom	previous	page

T (1 ()	1		continued ir	-			Cl (c)
Length $(\mu \mathbf{m})$	c-angle	\mathbf{D}_{par} ($\mu\mathbf{m}$)	\mathbf{D}_{per} ($\mu\mathbf{m}$)	Cl (apfu)	OH (apfu)	\mathbf{r}_{mr0}	eCl (apfu)
11.10	37.83	2.12	0.25	0.005	0.511	0.832	0.024
9.74	62.84	2.12	0.25	0.005	0.511	0.832	0.024
13.38	45.05	2.12	0.25	0.005	0.511	0.832	0.024
14.26	45.89	2.12	0.25	0.005	0.511	0.832	0.024
11.64	77.41	2.12	0.25	0.005	0.511	0.832	0.024
10.11	79.31	2.38	0.25	0.000	0.457	0.829	0.033
10.34	49.67	2.38	0.25	0.000	0.457	0.829	0.033
13.28	66.79	2.38	0.25	0.000	0.457	0.829	0.033
12.22	29.08	2.38	0.25	0.000	0.457	0.829	0.033
12.68	42.74	2.38	0.25	0.000	0.457	0.829	0.033
14.00	67.69	2.38	0.25	0.000	0.457	0.829	0.033
14.86	31.95	2.38	0.25	0.000	0.457	0.829	0.033
12.72	30.34	2.38	0.25	0.000	0.457	0.829	0.033
13.32	55.92	2.38	0.25	0.000	0.457	0.829	0.033
11.20	82.70	2.38	0.25	0.000	0.457	0.829	0.033
13.10	84.15	2.38	0.25	0.000	0.457	0.829	0.033
11.19	43.92	2.38	0.25	0.000	0.457	0.829	0.033
10.15	60.10	2.38	0.25	0.000	0.457	0.829	0.033
15.30	36.91	1.52	0.31	0.003	0.351	0.846	-0.018
14.36	53.66	1.52 1.52	0.31	0.003	0.351	0.846	-0.018
14.50 10.51	43.72	$\frac{1.52}{1.52}$	0.31	0.003	0.351 0.351	0.846	-0.018
12.55	64.24 71.75	1.52	0.31	0.003	0.351	0.846	-0.018
12.17		2.07	0.40	0.000	0.437	0.841	-0.002
10.71	53.05	2.07	0.40	0.000	0.437	0.841	-0.002
10.16	57.97	2.07	0.40	0.000	0.437	0.841	-0.002
12.23	59.34	2.07	0.40	0.000	0.437	0.841	-0.002
12.00	79.57	1.68	0.33	0.011	0.475	0.834	0.018
15.01	40.93	1.68	0.33	0.011	0.475	0.834	0.018
12.25	65.35	1.68	0.33	0.011	0.475	0.834	0.018
13.09	44.99	1.68	0.33	0.011	0.475	0.834	0.018
14.57	36.83	1.68	0.33	0.011	0.475	0.834	0.018
13.86	63.81	1.68	0.33	0.011	0.475	0.834	0.018
12.84	58.77	1.68	0.33	0.011	0.475	0.834	0.018
13.09	41.30	1.68	0.33	0.011	0.475	0.834	0.018
10.07	74.88	1.68	0.33	0.011	0.475	0.834	0.018
8.33	81.49	1.68	0.33	0.011	0.475	0.834	0.018
15.14	30.75	1.68	0.33	0.011	0.475	0.834	0.018
15.09	12.39	1.68	0.33	0.011	0.475	0.834	0.018
9.54	71.85	1.68	0.33	0.011	0.475	0.834	0.018
10.86	44.73	1.93	0.33	0.006	0.429	0.830	0.031
10.69	44.58	1.93	0.33	0.006	0.429	0.830	0.031
14.40	65.47	1.93	0.33	0.006	0.429	0.830	0.031
8.93	59.65	1.93	0.33	0.006	0.429	0.830	0.031
11.39	49.56	1.93	0.33	0.006	0.429	0.830	0.031
11.06	40.22	1.93	0.33	0.006	0.429	0.830	0.031
11.40	69.41	1.93	0.33	0.006	0.429	0.830	0.031
14.38	44.83	1.93	0.33	0.006	0.429	0.830	0.031
13.56	48.66	1.93	0.33	0.006	0.429	0.830	0.031
14.36	33.55	1.92	0.27	0.006	0.515	0.818	0.062
10.91	46.66	1.92	0.27	0.006	0.515	0.818	0.062
11.34	47.30	1.92	0.27	0.006	0.515	0.818	0.062
11.86	69.88	1.92	0.27	0.006	0.515	0.818	0.062
13.26	33.85	1.92	0.27	0.006	0.515	0.818	0.062
13.13	32.96	1.92	0.27	0.006	0.515	0.818	0.062
12.65	57.08	1.92	0.27	0.006	0.515	0.818	0.062
13.68	44.01	1.92	0.27	0.006	0.515	0.818	0.062
13.84	74.92	1.92	0.27	0.006	0.515	0.818	0.062
12.47	53.07	1.92	0.27	0.006	0.515	0.818	0.062
13.43	68.59	1.92	0.27	0.006	0.515	0.818	0.062
vv		~-					

Table S5 continued from previous page

Length $(\mu \mathbf{m})$	c-angle	\mathbf{D}_{par} ($\mu\mathbf{m}$)	\mathbf{D}_{per} ($\mu\mathbf{m}$)	Cl (apfu)	OH (apfu)	\mathbf{r}_{mr0}	eCl (apfu)
12.61	50.04	1.92	0.27	0.006	0.515	0.818	0.062
12.94	49.43	1.92	0.27	0.006	0.515	0.818	0.062
14.27	79.21	1.92	0.27	0.006	0.515	0.818	0.062
13.71	67.87	1.90	0.25	0.002	0.479	0.832	0.025
13.49	44.86	1.90	0.25	0.002	0.479	0.832	0.025
14.56	17.28	1.90	0.25	0.002	0.479	0.832	0.025
12.04	77.14	1.90	0.25	0.002	0.479	0.832	0.025
11.25	37.96	1.90	0.25	0.002	0.479	0.832	0.025
12.75	45.60	1.90	0.25	0.002	0.479	0.832	0.025
15.30	12.79	1.90	0.25	0.002	0.479	0.832	0.025
13.72	50.35	2.23	0.35	0.003	0.413	0.842	-0.004
11.07	68.64	2.13	0.28	0.006	0.517	0.821	0.055
10.80	54.43	2.13	0.28	0.006	0.517	0.821	0.055
14.20	40.05	2.13	0.28	0.006	0.517	0.821	0.055
10.51	47.08	2.13	0.28	0.006	0.517	0.821	0.055
16.36	37.69	2.13	0.28	0.006	0.517	0.821	0.055
11.09	39.89	2.13	0.28	0.006	0.517	0.821	0.055
14.85	61.05	2.13	0.28	0.006	0.517	0.821	0.055
15.27	50.85	2.13	0.28	0.006	0.517	0.821	0.055
10.82	75.57	2.13	0.28	0.006	0.517	0.821	0.055

MTL = 12.25 \pm 1.66 μ m (1 σ , n = 138) \pm 0.14 std. error. Skewness = -0.082; Kurtosis = -0.649. Mean D_{par} = 1.95 (4 etch figures each measurement); mean D_{per} = 0.29; analyst: POS.

References

- CP Sturrock, RM Flowers, FA Macdonald, The Late Great Unconformity of the Central Canadian Shield. Geochem. Geophys. Geosystems 22, e2020GC009567 (2021).
- 2. S Anderson, C Böhm, E Syme, A Carlson, L Murphy, Far North Geomapping Initiative: geological investigations in the Great Island area, Manitoba (parts of NTS 54L13, 54M4, 64I15, 16, 64P1, 2) in *Report of Activities 2009*. (Manitoba Geological Survey), pp. 132–147 (2009).
- 3. S Anderson, C Böhm, E Syme, Far North Geomapping Initiative: bedrock geological investigations in the Seal River region, northeastern Manitoba (parts of NTS 54L, M, 64I, P) in *Report of Activities 2010*. (Manitoba Innovation, Energy and Mines, Manitoba Geological Survey), p. 6–22 (2010).
- 4. N Rayner, Far North Geomapping Initiative: new U-Pb geochronological results from the Seal River region, northeastern Manitoba (parts of NTS 54L, M, 64I, P) in Report of Activities 2010. (Manitoba Innovation, Energy and Mines, Manitoba Geological Survey), pp. 23–35 (2010).
- 5. KT McDannell, RM Flowers, Vestiges of the Ancient: Deep-Time Noble Gas Thermochronology. *Elements* 16, 325–330 (2020).
- KT McDannell, DA Schneider, PK Zeitler, PB O'Sullivan, DR Issler, Reconstructing deep-time histories from integrated thermochronology: An example from southern Baffin Island, Canada. Terra Nova 31, 189–204 (2019).
- 7. P Vermeesch, Y Tian, Thermal history modelling: HeFTy vs. QTQt. Earth-Science Rev. 139, 279-290 (2014).
- 8. M Fox, DL Shuster, Lazed and Diffused: Untangling Noble Gas Thermochronometry Data for Exhumation Rates. *Elements* **16**, 337–342 (2020).
- 9. KT McDannell, DR Issler, Simulating sedimentary burial cycles Part 1: Investigating the role of apatite fission track annealing kinetics using synthetic data. *Geochronology* 3, 321–335 (2021).
- 10. KT McDannell, CB Keller, WR Guenthner, PK Zeitler, DL Shuster, Thermochronologic constraints on the origin of the Great Unconformity. *Proc. Natl. Acad. Sci.* 119, e2118682119 (2022).
- 11. KT McDannell, PK Zeitler, DA Schneider, Instability of the southern Canadian Shield during the late Proterozoic. *Earth Planet. Sci. Lett.* **490**, 100–109 (2018).
- 12. RM Flowers, RA Ketcham, DL Shuster, KA Farley, Apatite (U-Th)/He thermochronometry using a radiation damage accumulation and annealing model. *Geochimica et Cosmochimica Acta* 73, 2347–2365 (2009).
- 13. RA Ketcham, C Gautheron, A Recanati, M Rahn, Possible influence of alpha recoil track percolation on helium diffusivity in apatite in *Goldschmidt Abstracts*. (Geochemical Society, Paris, France), p. 1983 (2017).
- 14. A Recanati, et al., Helium trapping in apatite damage: Insights from (U-Th-Sm)/He dating of different granitoid lithologies. *Chem. Geol.* 470, 116–131 (2017).
- 15. KT McDannell, DR Issler, PB O'Sullivan, Radiation-enhanced fission track annealing revisited and consequences for apatite thermochronometry. *Geochimica et Cosmochimica Acta* **252**, 213–239 (2019).
- 16. RA Ketcham, Forward and Inverse Modeling of Low-Temperature Thermochronometry Data. Rev. Mineral. Geochem. 58, 275–314 (2005).
- 17. B Sanford, Paleozoic Geology of the Hudson Platform in *Sedimentary Basins and Basin-Forming Mechanisms*, eds. C Beaumont, A Tankard. (Canadian Society of Petroleum Geologists) Vol. Memoir 12, pp. 483–505 (1987).
- 18. BV Sanford, AC Grant, New findings relating to the stratigraphy and structure of the Hudson Platform in *Current Research Part D, Interior Plains and Arctic Canada*. (Geological Survey of Canada) Vol. 90-1D, pp. 17–30 (1990).
- 19. A Norris, Hudson Platform Geology in Sedimentary Cover of the Craton in Canada, eds. D Stott, J Aitken. (The Geological Society of America), pp. 653–700 (1993).
- J Burrus, et al., A two-dimensional regional basin model of Williston Basin hydrocarbon systems. AAPG Bull. 80, 265–291 (1996).
- 21. TS White, BJ Witzke, GA Ludvigson, Evidence for an Albian Hudson arm connection between the Cretaceous Western Interior Seaway of North America and the Labrador Sea. Geol. Soc. Am. Bull. 112, 1342–1355 (2000).
- 22. K Osadetz, B Kohn, S Feinstein, P O'Sullivan, Thermal history of Canadian Williston basin from apatite fission-track thermochronology—implications for petroleum systems and geodynamic history. *Tectonophysics* **349**, 221–249 (2002).
- 23. N Pinet, D Lavoie, J Dietrich, K Hu, P Keating, Architecture and subsidence history of the intracratonic Hudson Bay Basin, northern Canada. *Earth-Science Rev.* **125**, 1–23 (2013).
- 24. PJ Rousseeuw, Least Median of Squares Regression. J. Am. Stat. Assoc. 79, 871-880 (1984).
- 25. P Wessel, et al., The Generic Mapping Tools Version 6. Geochem. Geophys. Geosystems 20, 5556-5564 (2019).
- 26. K Gallagher, Transdimensional inverse thermal history modeling for quantitative thermochronology. J. Geophys. Res. Solid Earth 117 (2012).
- 27. K Gallagher, RA Ketcham, Comment on "Thermal history modelling: HeFTy vs. QTQt" by Vermeesch and Tian, Earth-Science Reviews (2014), 139, 279–290. Earth-Science Rev. 176, 387–394 (2018).
- 28. K Gallagher, RA Ketcham, Comment on the reply to the Comment on "Thermal history modelling: HeFTy vs. QTQt" by Vermeesch and Tian, Earth-Science Reviews (2014), 139, 279–290. Earth-Science Rev. 203, 102878 (2020).
- 29. SE Peters, JM Husson, J Czaplewski, Macrostrat: A platform for geological data integration and deep-time earth crust research. *Geochem. Geophys. Geosystems* 19, 1393–1409 (2018).
- 30. D Lavoie, et al., Hudson Bay, Hudson Strait, Moose River, and Foxe basins: synthesis of the research activities under the Geomapping for Energy and Minerals (GEM) programs 2008-2018, (Geological Survey of Canada, Open File 8507),

- Technical report (2019).
- 31. FM Gradstein, JG Ogg, MD Schmitz, GM Ogg, eds., The Geologic Timescale 2012. (Elsevier), pp. 1–1176 (2012).
- 32. FM Gradstein, JG Ogg, MD Schmitz, GM Ogg, eds., Geologic Time Scale 2020. (Elsevier), pp. 1–1357 (2020).
- 33. SJ Nelson, Ordovician paleontology of the northern Hudson Bay lowland. Mem. Geol. Soc. Am. 90, 1–145 (1963).
- 34. DK Armstrong, MPB Nicolas, KE Hahn, D Lavoie, Stratigraphic synthesis of the Hudson Platform in Manitoba, Ontario, and Nunavut: Ordovician-Silurian, (Geological Survey of Canada, Open File 8378), Technical report (2018).
- 35. S Zhang, JF Riva, The stratigraphic position and the age of the Ordovician organic-rich intervals in the northern Hudson Bay, Hudson Strait, and Foxe basins—evidence from graptolites. Can. J. Earth Sci. 55, 897–904 (2018).
- 36. H Trettin, Investigations of Lower Paleozoic geology, Foxe Basin, northeastern Melville Peninsula, and parts of northwestern and central Baffin Island. *Geol. Surv. Can. Bull.* **251**, 1–171 (1975).
- 37. RD LeFever, Sedimentology and Stratigraphy of the Deadwood-Winnipeg Interval (Cambro-Ordovician), Williston Basin in *Paleozoic Systems of the Rocky Mountain Region*, eds. M Longman, M Sonnenfeld. (Rocky Mountain Section, Society for Sedimentary Geology), pp. 11–28 (1996).
- 38. M Nicolas, Phanerozoic stratigraphic correlation chart for Manitoba, (Manitoba Agriculture and Resource Development, Manitoba Geological Survey, Open File OF2020-7), Technical report (2020).
- 39. R McKay, E Enkelmann, T Hadlari, W Matthews, F Mouthereau, Cenozoic Exhumation History of the Eastern Margin of the Northern Canadian Cordillera. *Tectonics* **40** (2021).
- 40. P Vermeesch, IsoplotR: A free and open toolbox for geochronology. Geosci. Front. 9, 1479–1493 (2018).
- 41. JK Hourigan, PW Reiners, MT Brandon, U-Th zonation-dependent alpha-ejection in (U-Th)/He chronometry. *Geochimica et Cosmochimica Acta* **69**, 3349–3365 (2005).
- 42. RA Ketcham, C Gautheron, L Tassan-Got, Accounting for long alpha-particle stopping distances in (U-Th-Sm)/He geochronology: Refinement of the baseline case. *Geochimica et Cosmochimica Acta* 75, 7779–7791 (2011).
- 43. PW Reiners, TL Spell, S Nicolescu, KA Zanetti, Zircon (U-Th)/He thermochronometry: He diffusion and comparisons with 40Ar/39Ar dating. *Geochimica et Cosmochimica Acta* **68**, 1857–1887 (2004).
- 44. PW Reiners, S Nicolescu, Measurement of parent nuclides for (U-Th)/He chronometry by solution sector ICP-MS, Technical report (2006).
- 45. KJ Dobson, FM Stuart, TJ Dempster, U and Th zonation in Fish Canyon Tuff zircons: Implications for a zircon (U-Th)/He standard. Geochimica et Cosmochimica Acta 72, 4745–4755 (2008).
- 46. P Boehnke, TM Harrison, A meta-analysis of geochronologically relevant half-lives: Whats the best decay constant? *Int. Geol. Rev.* **56**, 905–914 (2014).
- 47. A Gleadow, M Harrison, B Kohn, R Lugo-Zazueta, D Phillips, The Fish Canyon Tuff: A new look at an old low-temperature thermochronology standard. *Earth Planet. Sci. Lett.* **424**, 95–108 (2015).
- 48. MD Schmitz, SA Bowring, U-Pb zircon and titanite systematics of the Fish Canyon Tuff: an assessment of high-precision U-Pb geochronology and its application to young volcanic rocks. *Geochim. Cosmochim. Acta* **65**, 2571–2587 (2001).
- PR Renne, et al., Intercalibration of standards, absolute ages and uncertainties in 40Ar/39Ar dating. Chem. Geol. 145, 117–152 (1998).
- 50. FW McDowell, WC McIntosh, KA Farley, A precise 40Ar-39Ar reference age for the Durango apatite (U-Th)/He and fission-track dating standard. *Chem. Geol.* **214**, 249–263 (2005).
- 51. RA Ketcham, A Carter, RA Donelick, J Barbarand, AJ Hurford, Improved modeling of fission-track annealing in apatite. Am. Mineral. 92, 799–810 (2007).
- 52. WD Carlson, RA Donelick, RA Ketcham, Variability of apatite fission-track annealing kinetics: I. Experimental results. *Am. Mineral.* **84**, 1213–1223 (1999).
- 53. P Vermeesch, Statistics for LA-ICP-MS based fission track dating. Chem. Geol. 456, 19–27 (2017).
- 54. RA Ketcham, P van der Beek, J Barbarand, M Bernet, C Gautheron, Reproducibility of Thermal History Reconstruction From Apatite Fission-Track and (U-Th)/He Data. *Geochem. Geophys. Geosystems* 19, 2411–2436 (2018).
- 55. P Vermeesch, Statistics for Fission-Track Thermochronology in Fission-Track Thermochronology and its Application to Geology, eds. MG Malusa, P Fitzgerald. (Springer International Publishing, New York), 1 edition, pp. 109–122 (2019).
- 56. KT McDannell, Notes on statistical age dispersion in fission-track datasets: the chi-square test, annealing variability, and analytical considerations. *EarthArXiv*, 1–4 (2020).
- 57. RF Galbraith, Statistics for fission track analysis. (Chapman and Hall/CRC, Taylor and Francis Group, Boca Raton, FL), pp. 1–219 (2005).
- 58. JS Stacey, JD Kramers, Approximation of terrestrial lead isotope evolution by a two-stage model. *Earth Planet. Sci. Lett.* **26**, 207–221 (1975).
- 59. DR Issler, KT McDannell, PB O'Sullivan, LS Lane, Simulating sedimentary burial cycles Part 2: Elemental-based multikinetic apatite fission-track interpretation and modelling techniques illustrated using examples from northern Yukon. *Geochronology* 4, 373–397 (2022).